Solid-state rigid-rod polymer composite electrolytes with nanocrystalline lithium ion pathways

*Ying Wang[1], Curt J. Zanelotti[1], Xiaoen Wang[2], Robert Kerr[2], Liyu Jin[2], Wang Hay Kan[3], Theo J. Dingemans[4], Maria Forsyth[2], and Louis A. Madsen[1]**

1. Department of Chemistry and Macromolecules Innovation Institute
   Virginia Polytechnic Institute and State University
   Blacksburg, Virginia 24061, United States
   E-mail: lmadsen@vt.edu
2. Institute for Frontier Materials and ARC Centre of Excellent for Electromaterials Science
   Deakin University
   Geelong, VIC 3216, Australia
3. China Spallation Neutron Source
   Chinese Academy of Science
   Dongguan, Guangzhou 523803, China
4. Department of Applied Physical Sciences
   University of North Carolina at Chapel Hill
   121 South Road, Chapel Hill, NC27599-3050, United States

Abstract

A critical challenge for next-generation lithium-based batteries lies in development of electrolytes that enable thermal safety along with use of high-energy-density electrodes. We describe molecular ionic composite (MIC) electrolytes based on an aligned liquid crystalline polymer combined with ionic liquids and concentrated Li salt. This high strength (200 MPa) and non-flammable solid electrolyte possesses outstanding Li^+ conductivity (1 $mS \cdot cm^{-1}$ at 25 °C) and electrochemical stability (5.6 V vs $Li|Li^+$) while suppressing dendrite growth and exhibiting low interfacial resistance (32 $\Omega \cdot cm^2$) and overpotentials ($\leq$ 120 mV @ 1 $mA \cdot cm^{-2}$) during Li symmetric cell cycling. A heterogeneous salt doping process modifies a locally ordered polymer-ion assembly to incorporate an inter-grain network filled with defective LiFSI & $LiBF_4$ nanocrystals, strongly enhancing Li^+ conduction. This modular material fabrication platform shows promise for safe and high-energy-density energy storage and conversion applications, incorporating the fast transport of ceramic-like conductors with the superior flexibility of polymer electrolytes.

Solid-state polymer electrolytes (SPEs) have received great attention toward reviving high-energy-density Li-based batteries.[1-4] While Li-ion batteries play an important role in the energy storage landscape due to their relatively high specific energy and power density, they are approaching theoretical limits (≈ 400 $Wh.kg^{-1}$).[5,6] In order to increase capacity of Li-based batteries, researchers have largely focused on new electrode materials. Regarding cathodes, Li-air and Li-sulfur batteries represent leading frontier candidates.[3,7-9] At the anode, Li-metal can replace graphite to increase anode energy density by ~ 10 fold.[5-7] However, electrode advancements require an enabling electrolyte to combat irreversible reactions and dendrite growth during long-term charge/discharge cycling.[7,10] To alleviate these issues, SPEs not only provide mechanical stiffness to block dendrites, but deliver safer (non-flammable) operation compared to liquid electrolytes.[1,10-12] Herein, we describe a solid-state ***molecular ionic composite*** (MIC) electrolyte[1,13-15] based on an extremely rigid double helical sulfonated aromatic polyamide (similar to Kevlar®)[16,17] combined with an ionic liquid (IL) and a Li salt. We can adjust MIC properties widely by changing polymer content, IL type, and metal salt type and loading. Thus, MICs represent a modular material platform with potential to resolve a range of issues in electrolytic materials.

Previous researchers have developed a number of IL-based gel electrolytes (termed “ion gels” or “ionogels”) that combine the non-flammability of ILs with a mechanically supporting matrix.[1,18-21] These electrolytes consist of either a polymer matrix embedded with a large volume fraction of IL,[1,22] or an IL inside an inorganic matrix such as SiO_2 and TiO_2.[19,20,23] Potential applications of these gels for high-energy-density Li batteries have been substantially explored.[20,24,25] However, these gels only show practical Li-metal cycling performance when doped with organic electrolytes,[20,25] which improve conductivity but introduce a volatile liquid

that diminishes safety against overheating and fire.[5,6] In this work, we describe solid-state MIC electrolytes that contain no volatile solvents but exhibit high ionic conductivity, beneficial electrode-electrolyte contact and high thermal stability, all while possessing sufficient modulus to serve as the separator in Li-metal batteries. Loading electrolytes with Li salts serves to increase Li-ion conductivity and supply Li^+ for reactions at the electrodes.[2,26-28] Maier et al. have demonstrated that heterogeneous doping and interfacially controlled materials can be used to increase Li^+ conductivity in electrolytes.[10] Christie et al. reported that the presence of the irregularly shaped bis(trifluoromethanesulfonyl)imide ($TFSI^-$) anion disrupts the electrostatic potential around Li^+ thereby enhancing ionic conductivity in a manner analogous to inorganic electrolytes such as $AgBr_{1-x}I_x$.[2] Recently, lithium bis(fluorosulfonyl)imide (LiFSI) has emerged as a promising electrolyte component.[28-30] Furthermore, the FSI^- anion can decompose upon electroreduction to form a stable solid-electrolyte interphase (SEI) that enables reversible cycling with a graphitic anode.[31] In this project, we employ ionic liquid electrolytes (ILEs) containing *N*-propyl-*N*-methylpyrrolidinium (C_3mpyr) FSI mixed with LiFSI ($\leq$ 3.2 mol/kg), which have previously shown Li-metal cycling at high rates.[32,33] By incorporating this ILE into a solid MIC, we demonstrate a highly lithium-dense solid-state electrolyte with potential to suppress Li dendrite growth on Li-metal anodes, enable fast Li^+ transport, and eliminate battery safety concerns.

The Li-loaded MIC (LiMIC) fabrication process requires two steps: (1) Initial polymer-IL network formation, followed by (2) ILE ion exchange to achieve high Li^+ loading. As shown in **Fig. 1a**, we obtain the raw MIC (RMIC), based on an interfacial ion-exchange process between a sulfonated aromatic polyamide, poly-2,2′-disulfonyl-4,4′-benzidine terephthalamide (Li-form PBDT) in H_2O solution and an IL, C_2mimBF_4 (1-ethyl-3-methylimidazolium tetrafluoroborate).[1]

PBDT is water-miscible and forms a highly ordered lyotropic nematic liquid crystal (LC) phase at concentrations > 2 wt%.[16,17] The local parallel packing of charged PBDT rods serves as the assembly template – not only offering mechanical integrity, but also endowing nanoscale structuring in the composite. RMICs are denoted with RMIC-5 and RMIC-15, in which the numbers denote PBDT weight percentage of 5% and 15%. In **Fig. 1b**, we immerse the rigorously dried RMICs in the desired ILE, i.e., C_3mpyrFSI with 50 mol% LiFSI. This serves the dual purposes of lowering the concentration of BF_4^- anions through ion-exchange while also introducing Li^+ ions into the polymer host matrix. By following this two-step fabrication method, we obtain a solid-state MIC electrolyte, denoted LiMIC-5 and LiMIC-15. The key to *Step 1* is that both the IL and LC polyelectrolyte dissolve in the same solvent. *Step 2* allows us to exchange a wide range of IL and Li salt mixtures into the MIC matrix and tailor properties of the product toward Li-metal batteries or other applications. The SEM images of RMICs (**Fig. 1c, d**) show locally aligned PBDT LC grains (μm-scale) interspersed with interconnected grain boundaries with a wide size distribution from nm - μm. This RMIC has mechanical cohesion propagated by a collective "electrostatic network," which effectively arises from templating of the IL through the highly charged and rigid double helical PBDT rods.[13,15] The RMICs are macroscopically isotropic, but display local alignment originating from the rigid PBDT chains, which can be verified using polarized optical microscopy (**Supplementary Fig. 1)**.[1,17]

Fig. 1e-g illustrates the concepts involved in multi-scale organization of the LiMICs. **Fig. 1e** shows the μm-scale structure of this solid electrolyte, incorporating aligned PBDT grains interleaved with a nanocrystalline ionic phase. These nanocrystalline grain boundaries serve as an additional conductive network providing fast Li^+ transport. As shown in **Fig. 1f**, we propose that after ion exchange with ILE, the interconnected boundaries separating the individual PBDT

grains allow for higher Li^+ density and faster Li^+ transport as compared to within the grains. **Fig. 1g** further illustrates the morphology and ion distribution in the internally aligned PBDT grains and the nanocrystalline component formed at the grain boundaries. We will illustrate this model in more detail in the following sections based on multi-modal material characterizations.

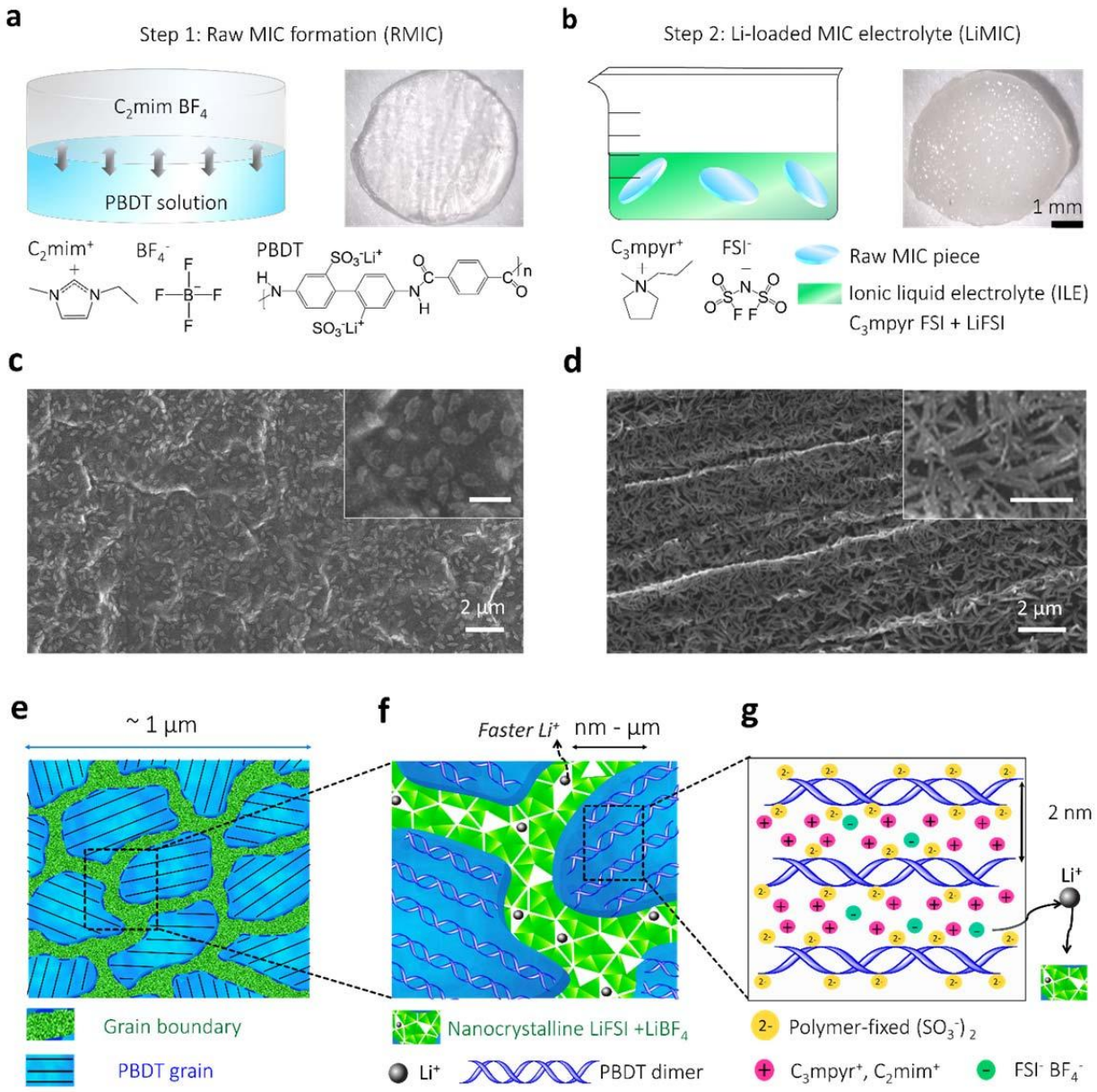

Figure 1. Fabrication processes to form Li-loaded MIC electrolytes (LiMICs). (a) ***Step 1*** shows fabrication of the raw MIC (RMIC). Mechanical cohesion in this RMIC arises via

electrostatic interactions,[1,13,15] and we obtain this material based on an interfacial ion exchange between a water-soluble IL (e.g., C_2mimBF_4) and an aqueous rigid-rod polyelectrolyte solution (Li-form PBDT in H_2O). The photograph shows the sliced transparent RMIC sample. (b) ***Step 2*** shows the second ion exchange process wherein we immerse a sliced section of the RMIC into the ILE (C_3mpyrFSI with 50 mol% LiFSI). During the infiltration process, the cation C_3mpyr^+ in the ILE tends to segregate into the PBDT-rich phase,[13,14] as the FSI^- and BF_4^- anions preferentially associate with Li^+ and precipitate out to form a nanoscale heterogeneous structure in the grain boundaries. The photograph shows the sliced iridescent LiMIC sample. (c,d) SEM images for RMIC-5(c) and RMIC-15(d). Higher magnification images are shown in the upper right insets. The scale bar for the insets is 1 μm. The interfaces between individual PBDT grains form the grain boundaries (darker regions). Both the aligned PBDT grains and the grain boundaries contain C_2mimBF_4. (e, f) After ***Step 2***, the grain boundaries become predominantly the condensed salt phase, which consists of nanocrystalline grains that form a conductive network supporting fast Li^+ transport. (g) The morphology of an aligned LC grain contains PBDT double helical rods filled predominantly with mobile IL cations. The distance between PBDT rods is ~ 2 nm.[1,15]

To investigate the nanoscale morphology of these composites, we conducted powder X-ray diffraction (XRD) experiments on the RMIC and LiMIC. As shown in **Fig. 2a**, we observe an amorphous halo with scattering angle 2θ from 12º to 30º for the RMIC, which we assign to the amorphous C_2mimBF_4 in the RMIC. A schematic picture is shown **in Fig. 2b**, where the locally aligned PBDT rods serve as the assembly template for the amorphous IL. The diffraction peaks of the PBDT are overwhelmed by the large volume fraction of IL in the RMIC. By contrast, the XRD of the LiMIC (**Fig. 2c**) shows a heterogeneous structure based on coexistence of the weak amorphous halo and the sharp crystalline reflections. This pattern agrees with the schematic picture shown in **Fig. 2d**, depicting a highly defective nanocrystalline domain formed in-situ between the PBDT grains in the LiMICs. The extracted 1D spectra are shown in **Fig. 2e**. The

crystalline peaks (blue line), at first glance, appear to be superimposed diffraction patterns of LiFSI and $LiBF_4$. We also notice that, compared to the amorphous phase, the crystalline phase is the dominant component in the LiMIC, which supports the solid-state NMR (SSNMR) integration results included in **Supplementary Table 1**, showing that ~ 80% anions (FSI^- and BF_4^-) in LiMIC are localized in the solid crystalline phase. We further use Le Bail refinement to determine the cell parameters for the two potential crystals.[34] **Fig. 2f** shows the fitting results with R-factor for the refinement R_p = 6.87%, which indicates good alignment between the observed diffraction patterns and the simulated phases of LiFSI and $LiBF_4$. The in-situ formed defective crystals of LiFSI and $LiBF_4$ possess preferred orientations, which contribute to the high density of vacancies that promote easier hopping of Li^+ between crystallites. We use the Scherrer equation[35] (**Supplementary Equation 1**) to determine the average crystallite size (19.4 nm) formed in the LiMIC grain boundary regions from the FWHM of the peak at $2\theta = 26.363^\circ$ (012) from the $LiBF_4$ phase. **Table 1** summarizes the Le Bail refinement with cell parameters for the two defective crystals, and both belong to the trigonal crystal structure. These results provide evidence that these nanocrystals are localized in the grain boundaries instead of within PBDT grains, where the distance between PBDT chains is too small to accomodate the nanocrystals.[1,15-17]

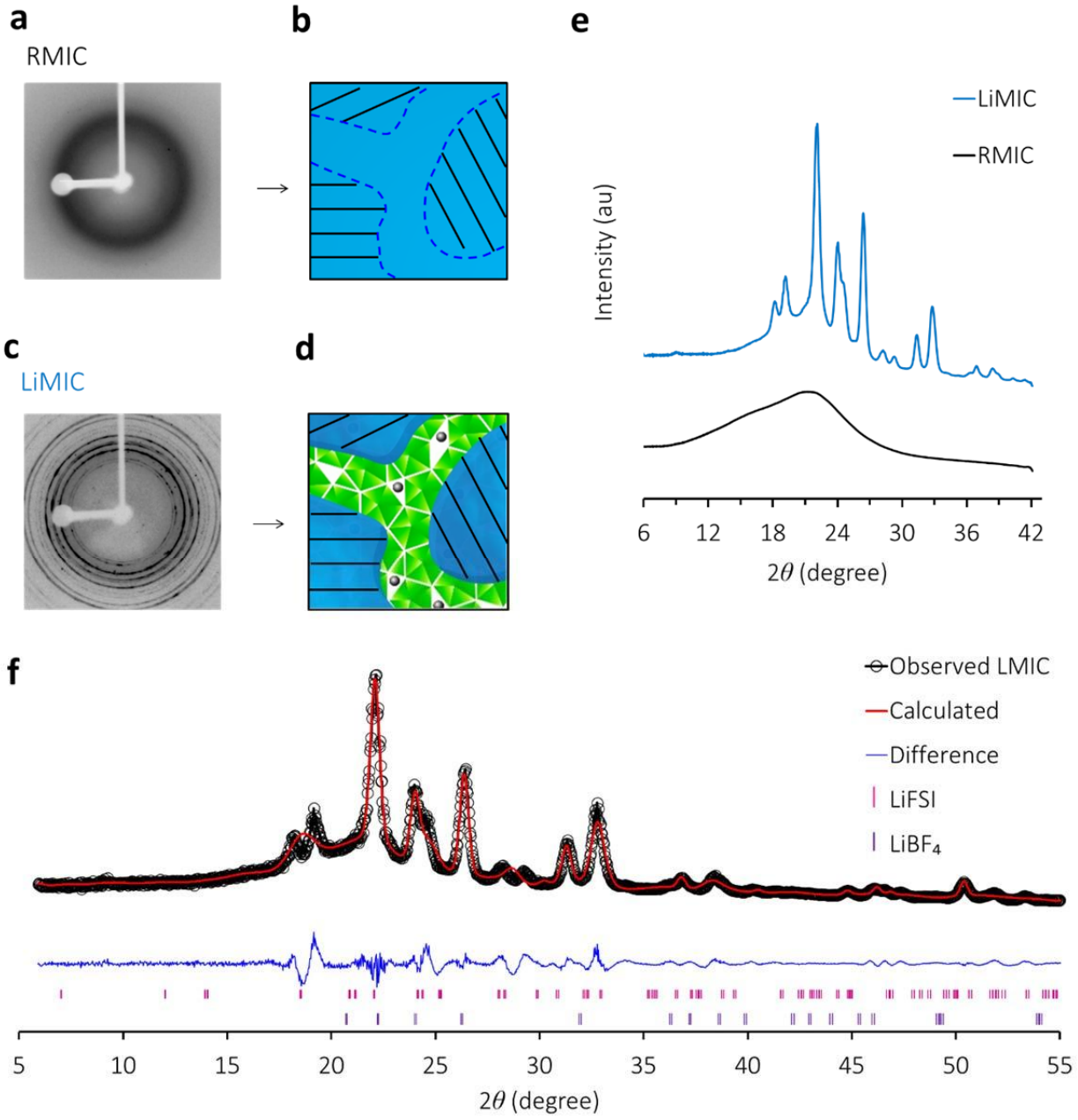

Figure 2. X-ray diffraction patterns of RMIC and LiMIC. (a) Powder XRD pattern for the RMIC. (b) In the RMIC, PBDT LC grains and grain boundaries are filled with amorphous IL as a result of ***Step 1*** of the fabrication process. (c) XRD pattern for the LiMIC. (d) In the LiMIC, there exists an in-situ formed and highly defective nanocrystalline structure between PBDT LC grains. (e) The extracted 1D spectra of the XRD images in (a) and (c). (f) Le Bail refinement results for the LiMIC XRD pattern, which include the observed pattern, the calculated results and the simulation of the in-situ formed nanocrystalline structure of LiFSI and $LiBF_4$.

Table 1. Li crystals formed in the LiMIC (R_{wp} = 9.75%, R_p = 6.87%)

LiMIC-15	Phase1 (LiFSI)	Phase2 ($LiBF_4$)
Crystal structure	**Trigonal**	**Trigonal**
Space group	P -3	P 31 2 1
a (Å) (α)	8.513 (90°)	4.9511(90°)
b (Å) (β)	8.513(90°)	4.9511(90°)
c (Å) (γ)	12.610 (120°)	11.112 (120°)
Volume($Å^3$)	779.76	228.02
ICSD	415618	171375

To understand the ion transport and morphology in both RMIC and LiMIC, we first verify the chemical composition of the products, qualitatively and quantitatively, based on ^1H, ^{19}F and ^7Li NMR spectroscopy. **Fig. 3a**, **b**, **c** present key features of these NMR studies. **Fig. 3a** shows ^1H spectra for C_2mim^+ in neat IL and C_3mpyr^+ in ILE (bottom two spectra), and compares ^1H spectra in the RMIC to the LiMIC. The linewidth in the LiMIC (~ 1500 Hz) is much broader compared to the RMIC (~ 100 Hz), which means a factor of ~ 15 faster T_2 spin-spin relaxation, indicating slower motion of IL cations. **Supplementary Fig. 2** shows additional ^1H spectra for RMIC-5 and RMIC-15. SSNMR offers promise for studying the same chemical species in distinct phases, including the grain boundaries and the locally aligned PBDT grains in LiMICs. **Fig. 3b** shows ^{19}F SSNMR spectra for LiMIC (blue line) along with spectra for the reference Li salts (LiFSI and $LiBF_4$). For the LiMIC, we observe a small percentage of mobile BF_4^- with a relatively narrow peak (light blue circle) at -150 ppm. The broad peak underneath (light green semicircle) refers to BF_4^- in the nanocrystalline grain boundaries. Due to its fast internal dynamics, FSI^- appears as only a singlet peak at 60 ppm, which we assign to the superposition of mobile FSI^- in aligned LC grains and solid FSI^- in nanocrystalline grain boundaries. The assignments, assumptions, and quantifications of different ionic species in the LiMICs are summarized in **Supplementary Fig. 3** and **Supplementary Table 1**. **Fig. 3c** compares ^7Li

spectra between ILE and LiMIC. The widths and integration values of the peaks are displayed in **Supplementary Fig. 4**. This single-component 3:4:3 splitting pattern indicates that Li^+ can only exist in either the crystalline grain boundaries or in the PBDT LC grains.[36,37] Based on the XRD, we observe that the Li^+ mainly forms into crystalline phases of LiFSI and $LiBF_4$ in the grain boundaries, thus demonstrating that Li^+ is the dominant cation in the solid nanocrystals, instead of in PBDT LC grains.

Understanding and controlling ion transport, ion associations and Li^+ transport mechanisms in electrolyte materials are critical for development of next-generation battery electrolytes. We can extract the diffusive activation energy (E_a) of the ions present in RMIC and LiMIC electrolytes based on the temperature dependencies of D_{Li^+}, $D_{cations}$ and D_{anions} obtained from NMR diffusometry as shown in **Fig. 3d,e**.[1,38-40] As indicated from the faster T_2 relaxation, we observe that D values for the mobile IL ions in LiMICs are an order of magnitude smaller than those in RMICs, as expected. **Fig. 3f** shows the extracted E_a values for cations and anions in RMICs and LiMICs via the Arrhenius equation. The E_a values for C_2mim^+ and BF_4^- increase with polymer content in the RMICs. This suggests that the density of the PBDT matrix dominates the local energetic barriers that govern ion transport. In addition, compared to the RMICs, the E_a values for cations in the LiMICs almost doubles, whereas E_a for anions show only a slight increment with polymer content. This indicates that the PBDT matrix escalates the local energetic barriers for cation transport in LiMICs, primarily because of stronger associations between the SO_3^- on PBDT chains and C_3mpyr^+. Correspondingly, the schematic picture for the trapped cations within the aligned LC grain is shown in **Fig. 3g.** Conversely, the E_a values for Li^+ in the LiMIC (**Fig. 3h**) decrease with increasing polymer content, indicating smaller local energetic barriers for Li^+ transport compared to the ILE.[13,40] This indicates that a different Li^+

transport mechanism applies for LiMICs. As shown in **Supplementary Table 1**, the concentration of mobile cations (C_2mim^+, C_3mpyr^+) and anions (FSI^-, BF_4^-) in the LiMICs are ~ 6 times lower compared to the RMICs. Meanwhile, LiMICs show an order of magnitude slower diffusion coefficients for the same set of mobile cations and anions. Based on the Nernst–Einstein equation, we suggest that the unexpectedly high conductivity observed in this solid LiMIC electrolyte (see below, Fig. 4a) originates from a fast Li^+ hopping ion transport mechanism in the solid nanocrystalline grain boundaries, as opposed to transport through a liquid-like mobile phase in the PBDT LC grains.[39,41,42] We further determine the Li^+ transference number determined by diffusion ($t_{Li^+\text{-NMR}}$) in LiMICs based on the **Supplementary Equation 2** and include the results in **Supplementary Table 1**. **Fig. 3i** depicts the nanocrystalline anions located in the grain boundaries, which we propose give rise to atypically fast Li^+ ion transport.

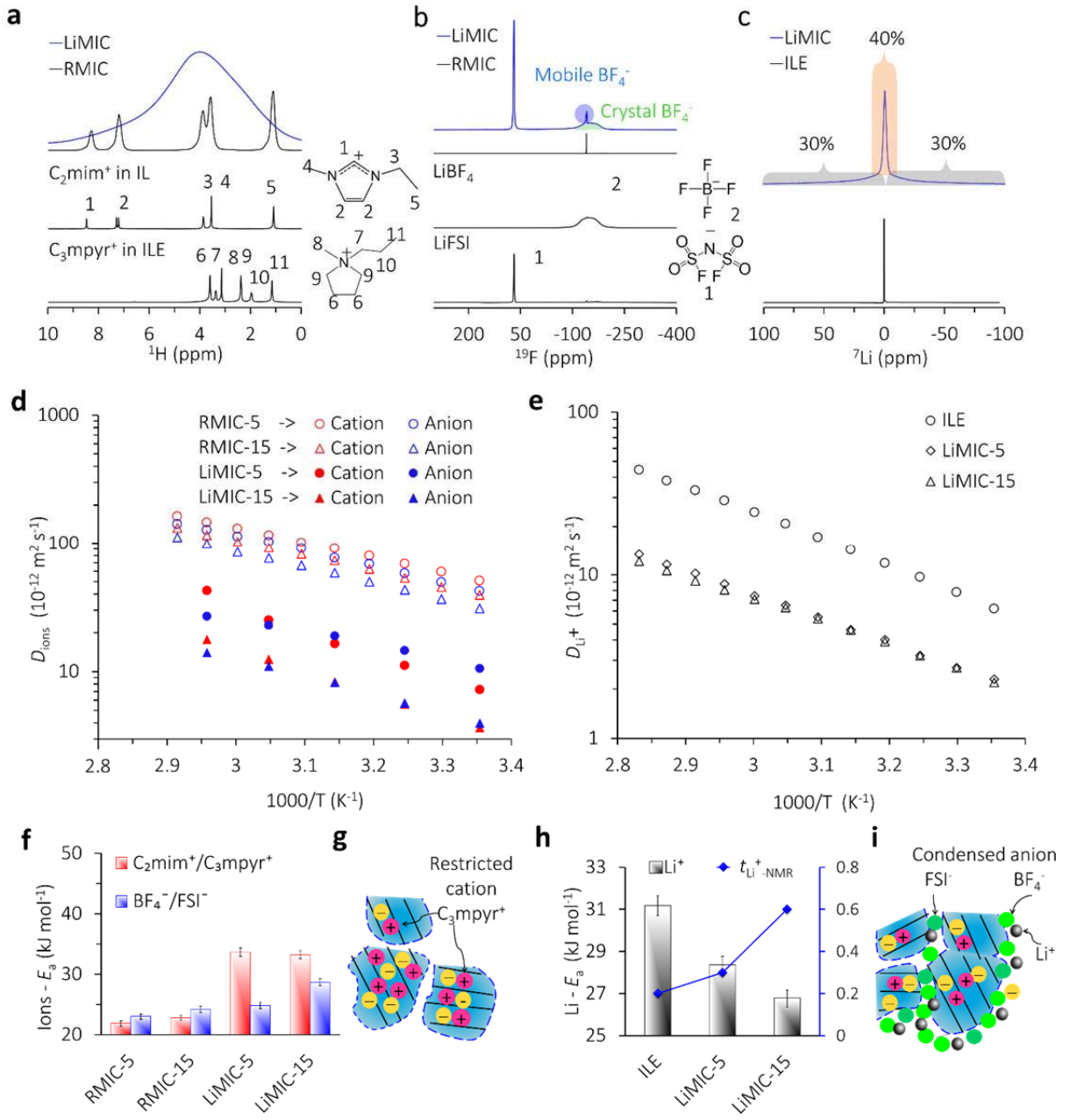

Figure 3. Chemical identification, diffusion coefficients, activation energies and transport mechanism in RMICs and LiMICs. (a) ^{1}H NMR spectra of cations in neat IL (C_2mimBF_4), ILE (C_3mpyrFSI with 50 mol% LiFSI), RMIC and LiMIC. The peak in the LiMIC shows overlapping C_3mpyr$^+$ and C_2mim$^+$ signals. (b) ^{19}F NMR spectra of solid LiFSI, solid $LiBF_4$, RMIC and LiMIC. (c) ^{7}Li spectra of liquid ILE and LiMIC. LiMIC shows single anisotropic environment with relative integration values of each broad satellite component being 30% and the narrow

central component being 40% due to the quadrupole splitting of Li. (d) Temperature-dependent $D_{cations}$ and D_{anions} in the RMICs and LiMIC. For LiMICs, $D_{cations}$ represents the average value for C_3mpyr^+ and C_2mim^+. The D_{anions} is the average value for mobile FSI^- and BF_4^-. D_{anions} is the computed weighted average value for the anions based on the mole ratio of mobile FSI^- and BF_4^- as quantified by ^{19}F NMR shown in **Supplementary Fig. 3** and **Supplementary Table 1**. (e) Temperature-dependent D_{Li^+} in ILE and LiMICs. (f) E_a values for cations and anions obtained from Arrhenius fitting of diffusion results. Uncertainties in diffusion are smaller than the marker and uncertainties in E_a are ≈ ±0.5 kJ/mol. (g) Schematic showing C_3mpyr^+ separations into locally aligned LC grains. (h) E_a values for Li^+ obtained from Arrhenius fitting. The blue line compares the measured $t_{Li^+\text{-NMR}}$ in ILE to that in LiMICs. (i) Schematic of the electrolyte structure showing the formation mechanism of nanocrystalline $LiBF_4$ and LiFSI in the grain boundaries.

Building on the RMIC morphology,[1] we propose that the formation mechanism for the heterogeneous structure in LiMICs lies in preferential associations and co-crystallization of specific ions. SO_3^- and C_3mpyr^+ ions should have the weakest associations with other ions due to their size and local charge distributions. Based on XRD and SSNMR results, we expect that FSI^- and BF_4^- have a strong affinity with Li^+ to form a thermodynamically favorable crystalline phase. These nanocrystals (20 nm) form within the grain boundaries when the concentration locally exceeds the saturation point of $LiBF_4$ and LiFSI in the ILE. This leaves the exchanged C_3mpyr^+ and residual C_2mim^+ cations to neutralize predominantly the polymer-fixed SO_3^- anions within the PBDT LC grains. The Li-rich nanocrystalline phase serves as a highly ion-conductive network that can transport Li^+. In these grain boundaries, the space-charge zone and nano-size effects among the polycrystalline $LiBF_4$, LiFSI and aligned crystalline PBDT grains should enhance the vacancy density and conductivity of Li^+, which is consistent with the decreasing E_a of Li^+ obtained from NMR diffusometry. We also note that this nanocrystalline phase likely exhibits features of plastic crystal behavior.[39,43-45] Further investigation of transport mechanisms,

grain boundary heterogeneities, space-charge effects and ion interactions in this heterogeneous structure will provide deeper understanding of these solid electrolytes for future materials design.

Fig. 4a shows ionic conductivities of LiMICs and RMICs as a function of temperature. The exceedingly high σ of LiMIC-5 (2.1 mS·cm^{-1}) and LiMIC-15 (1.5 mS·cm^{-1}) at 25°C surpasses that of state-of-the-art SPEs and even the liquid ILE (0.82 mS·cm^{-1}) we used for ion exchange in *Step 2*.[24,32] In terms of transport energy barriers, LiMICs show higher $E_a(\sigma)$ values compared to RMICs (**Fig. 4b**), which again indicates a distinct transport mechanism in LiMICs. We notice that E_a (Li^+-NMR) in LiMIC is close to the $E_a(\sigma)$ obtained from conductivity. This further indicates that the unexpectedly high conductivity in LiMICs originates from the nanocrystalline conductive network with an ionic alloy ($LiBF_4$ and LiFSI) that forms at the boundaries between individual grains. To supplement this demonstration, we determined the t_{Li}^+ based on the steady-state current of the Li symmetric cell assembled with LiMICs as electrolyte and separator in **Fig. 4c**. The corresponding impedance spectra of the cells before polarization are shown in **Supplementary Fig. 5**. The calculation details are included in **Supplementary Table 2** and **Equation S3**. The determined t_{Li}^+ in LiMIC-15 (0.60) is much higher compared to the ILE (t_{Li}^+ = 0.18).[32] One can then determine the fraction of conductivity due to Li^+ (σ_{Li}^+ = 1 mS cm^{-1}) in LiMICs by multiplying the overall conductivity by t_{Li}^+.

We also performed cyclic voltammetry to evaluate the Li plating (negative scan) and stripping (positive scan) behavior in LiMICs. As shown in the 1st cycle in **Fig. 4d**, upon scanning in the positive direction, the electrolyte shows no significant sign of electrochemical decomposition up to 5.6 V vs Li|Li^+. In addition, this electrolyte displays excellent cathodic stability for Li-metal cycling in the following cycles (2nd and 3rd cycles). In **Supplementary Fig. 6**, we observe that the columbic efficiency of LiMICs increases with cycle number, whereas the

ILE shows diminished performance, indicating more effective SEI formation on Li-metal anode when using LiMICs.

Next, we prepared Li|Li symmetric cells and recorded the voltage response for stepped current densities ranging from 0.01 $mA \cdot cm^{-2}$ to 1 $mA \cdot cm^{-2}$. **Fig. 4e** shows the voltage response for LiMIC-15 electrolytes. We observe that LiMIC-15 exhibits stable cycling and can withstand a current density (J) to 1 $mA \cdot cm^{-2}$. This represents state-of-the art performance for SPEs or IL-based electrolyte materials.[5,20] Overpotential is proportional to applied J **(Supplementary Fig. 7),** which follows the Butler-Volmer equation, thus avoiding the possibility of soft shorts.[5,33]

The LMIC electrolyte prepared with the ILE containing the highest concentration of LiFSI (3.2 mol kg^{-1}) shows the most stable cycling performance (**Supplementary Fig. 8** and **Supplementary Table 3**).[32,33] EIS spectra shown in **Fig. 4f** indicate that the SEI resistance increases over the first 40 cycles, then decreases upon further cycling and reduces below that of the initial state at 50 cycles. This is generally associated with an improving SEI layer that forms upon cycling and is commonly observed when cycling Li-metal in this ILE with high salt concentration. Notably, the interfacial resistance for this LiMIC-15 is unusually small, both before (32 $\Omega \cdot cm^{-2}$) and after (17 $\Omega \cdot cm^{-2}$) cycling, compared to other solid-state ion conductors, thereby overcoming the poor electrolyte-electrode contact between Li-metal anode and solid-ion conductor typically observed for, e.g., $Li_{10}GeP_2S_{12}$.[46]

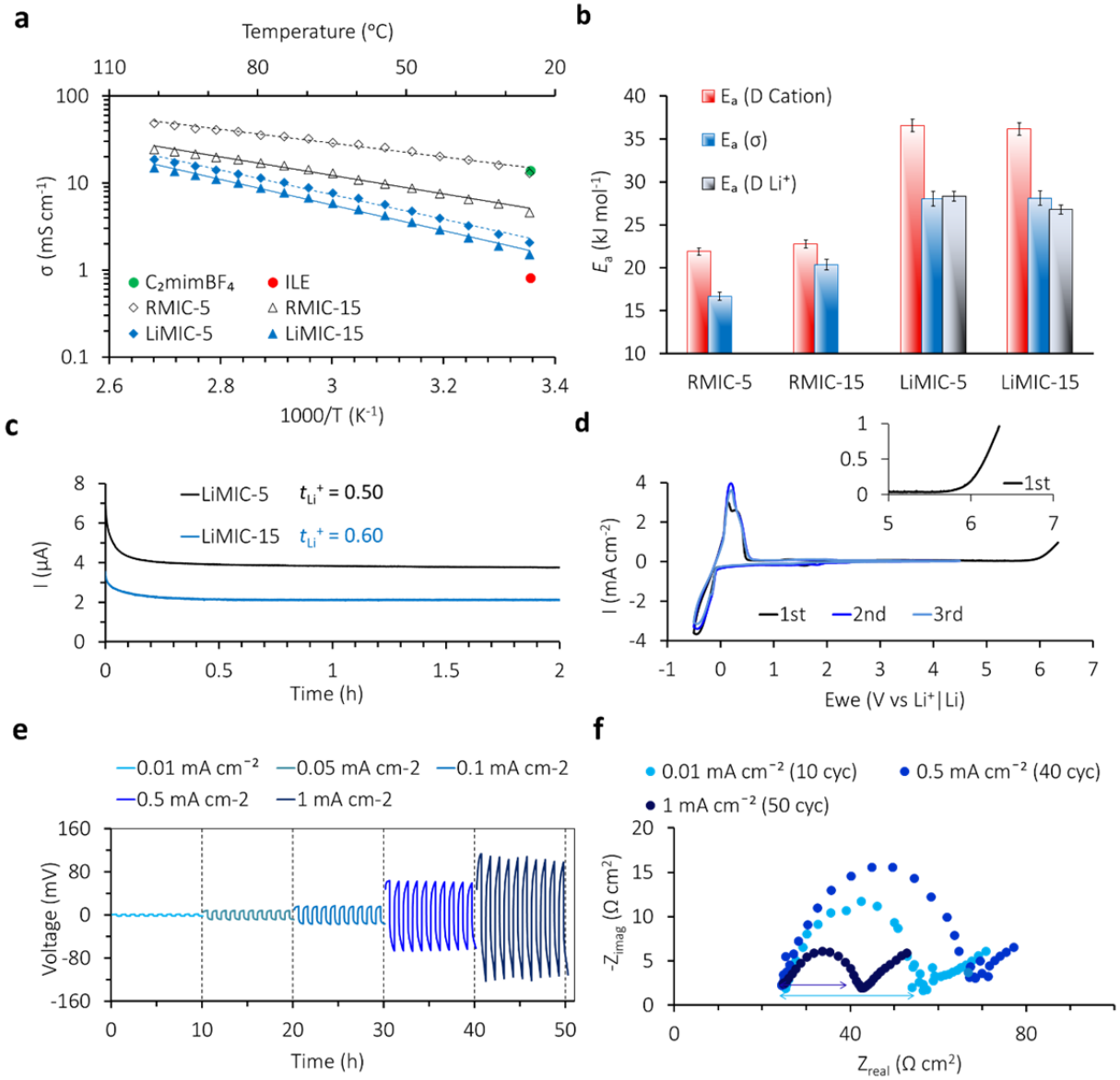

Figure 4. Ionic conductivity, activation energy, Li^+ transference number, electrochemical window, Li symmetric cell cycling performance, and interfacial charge-transfer resistance in MICs. (a) Arrhenius plot used to extract activation energies (E_a) for ionic conductivity within RMICs and LiMICs. The green dot shows the conductivity (σ) of C_2mimBF_4 (25 °C), used for developing RMICs. The ionic conductivity value in ILE is indicated with red dots. (b) Comparison of E_a values obtained from the conductivity results to E_a values of cations and Li^+ based on Arrhenius fitting of NMR diffusometry. (c) Steady-state current in symmetric Li|Li cell using LiMICs under 10 mV polarization. (d) Cyclic voltammetry curves for Li plating and stripping in LiMIC-15 at a sweep rate of 5 mV s^{-1}. Inset plot shows the enlarged view of the 1st cycle in the high voltage range. (e) Cell voltage versus time for a symmetric Li|Li cell using

LiMIC-15 at current densities (J) from 0.01 to 1 mA·cm^{-2} (each cycle lasts 1 h) with changes in J every 10 cycles. (f) Corresponding impedance spectra scanned before variation of J (10 cycles) for the LiMIC-15. The frequency range used is 1Hz – 1MHz.

In addition to the high Li^+ conductivity achieved by LiMICs, we also performed DSC and DMA to better understand their thermal and mechanical stability. As shown in **Fig. 5a**, DSC curves show that C_2mimBF_4 has been mostly exchanged or replaced in LiMICs after *Step 2* of ion exchange. In addition, we observe a glass transition (T_g = -75 °C) for LiFSI, which originates from the LiFSI phase, as reported in this ILE previously.[32,33] The enlarged view on the right displays a broad melting transition (T_m) of LiFSI in LiMICs, consistent with the XRD results showing that there exists a highly defective LiFSI crystalline phase in LiMICs. However, the T_m is not obvious, possibly originating from an endothermic melting process that has been offset by the exothermic degradation of LiFSI, as reported previously.[47] Meanwhile, we employed DMA to investigate the mechanical properties of RMICs and LiMICs between -50°C to 180°C, as shown in **Fig. 5b**. We observe that LiMIC-15 maintains high storage modulus (200 MPa) between -50 to 140 °C, which then drops above 140 °C, near the T_m of LiFSI as well as the degradation temperature for FSI^-.[47] During the heating process, the LiMIC modulus surpasses all previous state-of-the-art SPEs, which usually show poor mechanical strength at temperatures beyond the polymer T_g or T_m.[48] Flammability caused by formation of lithium dendrites represents another key obstacle to safe operation of Li-metal batteries. We included flammability testing results for RMIC in **Supplementary Fig. 9** and observe that RMICs are stable and cannot be ignited under a methane/O_2 flame. Additionally, we carried out nanoindentation experiments to study the microscopic modulus of the MIC materials (**Supplementary Fig. 10**), where we observe a large distribution of modulus values, reflecting the heterogeneous structure in LiMICs.

The median values shown in the boxplots indicate high consistency with macroscopic DMA results.

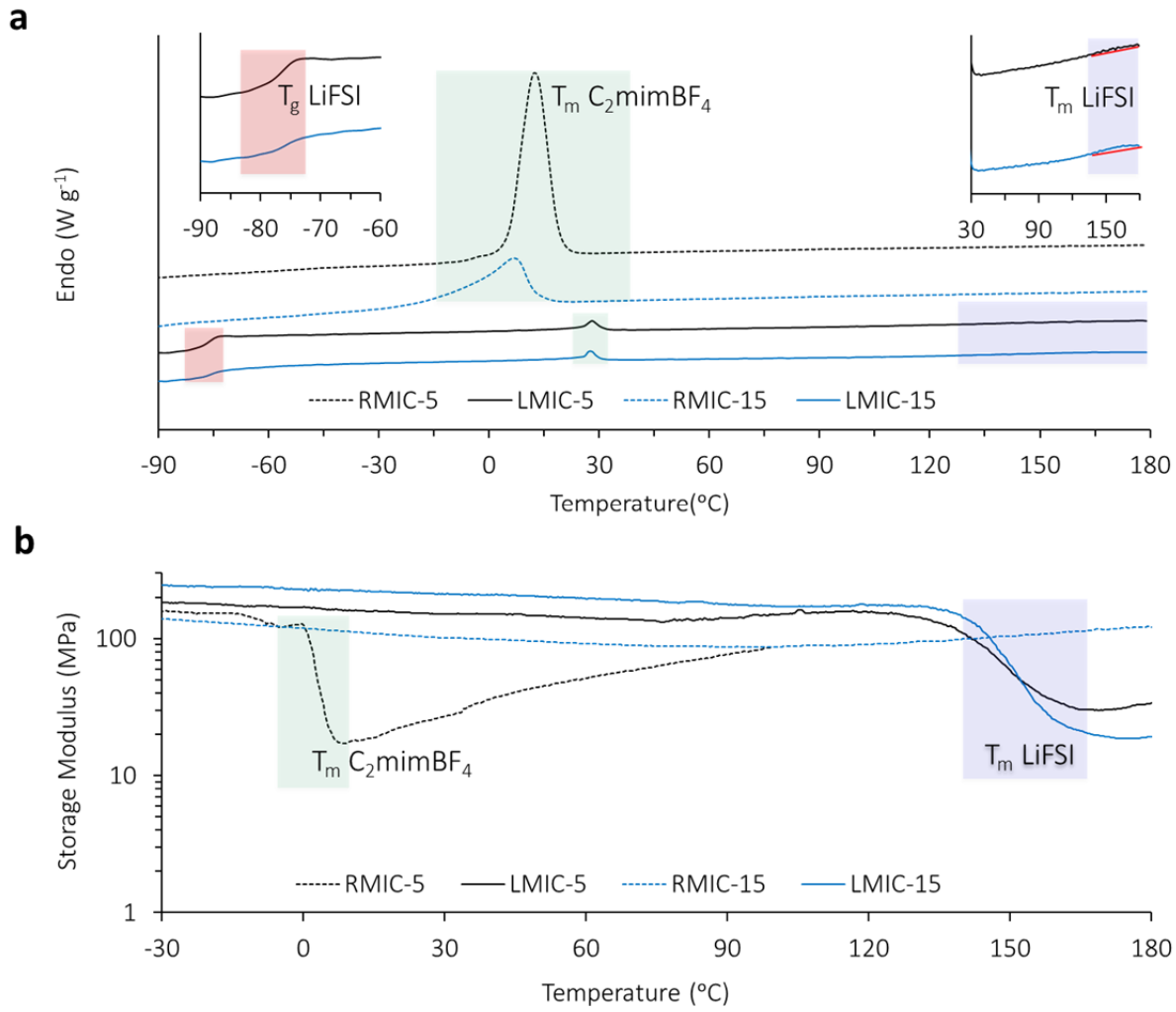

Figure 5. Thermal and mechanical properties of RMICs and LiMICs. (a) DSC shows apparent differences between LiMICs and RMICs. RMICs display the melting (T_m) of IL C_2mimBF_4 at 17 °C, whereas we only see a slight T_m peak for C_2mimBF_4 in LiMICs in agreement with the fact that C_2mimBF_4 has been largely exchanged out. According to peak integration analysis, only < 3% of C_2mimBF_4 remains in the LiMICs. Notably, we do not observe any apparent melting peaks belonging to $C_3mpyrFSI$ or $C_3mpyrBF_4$. The enlarged inset on the left shows the glass transition (T_g) at -75 °C, which originates from the in-situ formed and defective LiFSI phase. The enlarged inset on the right displays the broad melting transition (T_m) of LiFSI in LiMICs. The T_m peak is not obvious, likely because of the opposing thermal transition processes of melting and degradation of LiFSI. (b) DMA shows the mechanical

properties of RMICs and LiMICs from -30 °C to 180 °C. RMIC-5 shows a melting drop around the T_m of C_2mimBF_4. LiMICs maintain high modulus (200 MPa) between -50 to 140 °C then start dropping at 140 °C, which is near both the melting and degradation temperatures of LiFSI (140 °C).[47]

In addition to the cycling results in Fig. 4e, **Fig. 6a-b** shows long-term cycling performance of the LiMICs as a function of polymer content and current density (J). Based on comparison between LMIC-5 and LiMIC-15 at increasing J, (0.05, 0.1, 0.2 mA·cm^{-2}), we observe that LiMIC-15 (higher polymer content) shows longer cycling stability at all current densities. This suggests that Li dendrite growth is better suppressed by increasing the rigid polymer content. The discussion of short circuit behavior observed for LiMIC-5 is included in Note 10 of supplementary information. **Fig. 6c** demonstrates the cycling stability of LiMIC-15 at J = 0.2 mA·cm^{-2}. Here, we observe that the cell can cycle without short circuit for > 2000 cycles, which corresponds to 2000 h cycling time and thus removal (and re-plating) of an accumulated total of 1 mm thickness from each Li-metal electrode. Based on the falciform (curved) potential observed in the charging and discharging processes shown in the selected cycles across the long period, we do not observe the unstable voltage profile that typically exists in organic electrolytes at high rates.[32,33] Though overpotential is increasing, we can expect changes to the SEI layer formed on Li-metal during cycling, which is stable enough to suppress Li dendrite growth and prevent short-circuit. Post-cycling SEM of the Li-metal electrode surface (**Fig. 6d, e**) shows a smooth surface devoid of significant dendrites or 'mossy' lithium seen in typical organic electrolyte systems. Peaks from the breakdown products of the FSI^- anion can be seen in the EDX spectra (**Fig. 6f**), which are known to aid in chemically suppressing Li dendrites.[31]

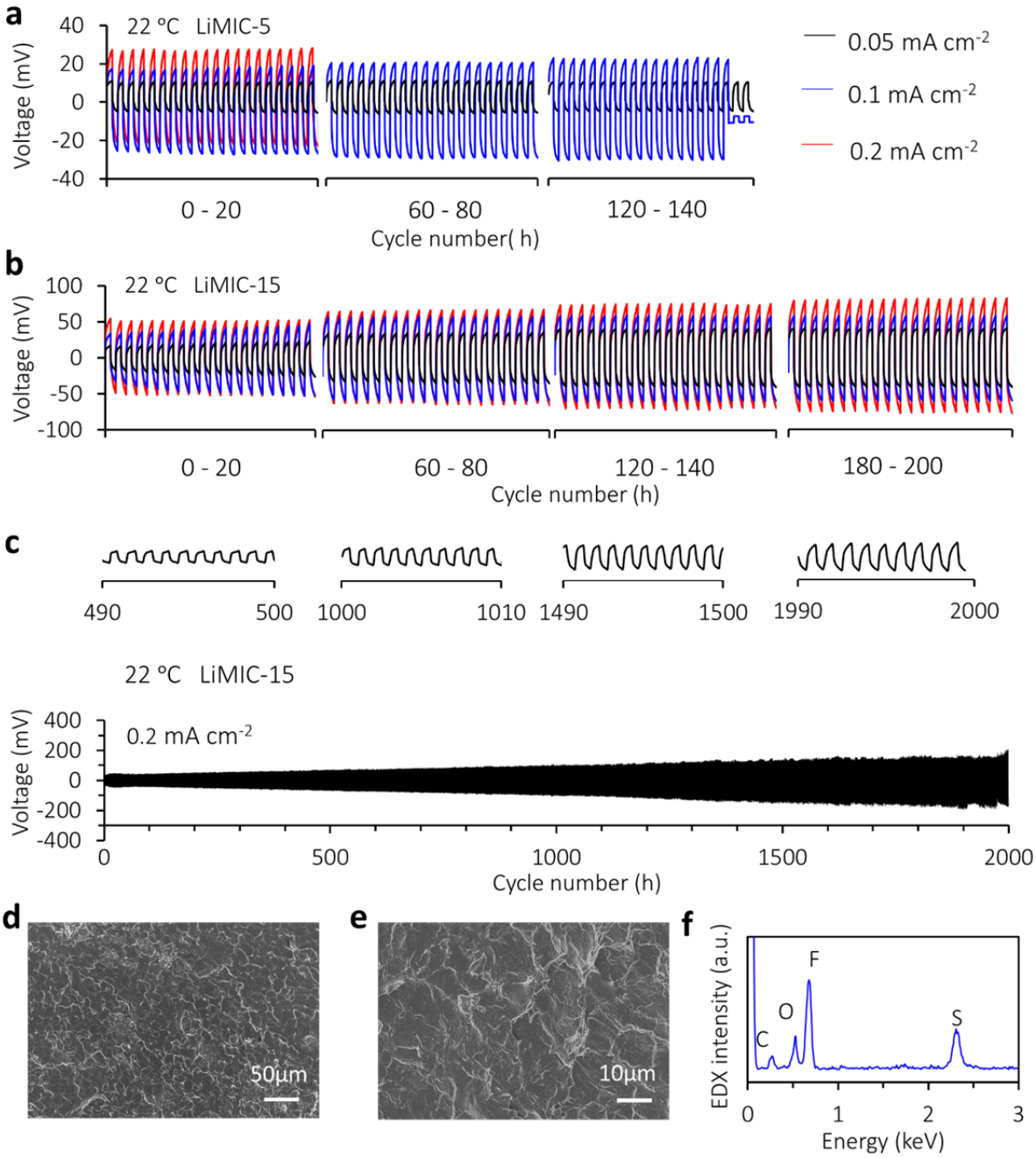

Figure 6. Voltage-time profiles for Li|Li symmetric cells incorporating LiMICs at ambient temperature. 1 cycle = 1 h, or 30 min for each charge and discharge. (a) 0.05 mA·cm^{-2}, 0.1 mA·cm^{-2} , 0.2 mA·cm^{-2} for LiMIC-5, (b) for LiMIC-15. (c) Long-term cycling of LiMIC-15 at current density of 0.2 mA·cm^{-2} with 1 h charge/discharge, insets are profiles for selected cycle numbers in the cycling period. (d, e) SEM images with different magnifications for the disassembled Li-metal electrode after 2000 h long-term cycling in (c) using LiMIC-15 as both electrolyte and separator. (f) EDX spectra of Li-metal surface after long-term cycling.

We have described materials development, mechanisms for ion transport, morphological self-assembly, as well as thermal, mechanical, and electrochemical properties of a new Li-loaded solid-state electrolyte. This inorganic/organic composite material shows immense potential to serve as a next-generation electrolyte for a range of electrochemical devices, suited for frontier battery technologies such as Li-metal, Li-S, or Na-based systems. The fabrication method described enables generation of non-flammable and highly conductive electrolytes with tunable modulus and with selectable metal ion type and varying concentrations. In addition to the initial component IL (C_2mimBF_4) described here, we can also fabricate MICs based on different combinations of ILs and PBDT. **Supplementary Table 4** summarizes the currently accessible MIC fabrication parameter space. Beyond batteries, MICs represent a modular material platform into which we can incorporate a wide range of ionic fluids and salts with an adjustable concentration of the highly charged and rigid double helical PBDT polymer. Such compositional freedom enables the fabrication of MICs with dramatic variations in chemical, mechanical, conductive, electrolytic, and thermal properties to enable applications in the next generation of safe and high-energy-density energy storage devices and beyond.

Methods

Materials: Poly 2,2′-disulfonyl-4,4′-benzidine terephthalamide (PBDT) was synthesized by interfacial condensation polymerization as described previously.[17,49] 1-ethyl-3-methyl imidazolium tetrafluoroborate (C_2mimBF_4, purity > 99%) was purchased from Solvent Innovation GmbH (Cologne, Germany). N-propyl-N-methylpyrrolidinium bis(fluorosulfonyl)imide (C_3mpyrFSI, purity > 99.9%) was purchased from Solvionic. Lithium bis(fluorosulfonyl)imide (LiFSI, purity >99.5%) was sourced from Suzhou Fluolyte Co., Ltd., China. Lithium metal was sourced from China Energy Lithium Co. Ltd. (purity > 99.9%). IL

electrolytes (ILEs) in this paper were prepared by adding the prescribed amount of LiFSI to C_3mpyrFSI IL at room temperature in an Ar-filled glove box (< 0 ppm O_2 and < 10 ppm H_2O).

Preparation of the RMIC: C_2mimBF_4 with the same volume as the (Li-counterion) PBDT seed aqueous solution was slowly pipetted on top of each solution. After 24 hours ion exchange, the hydrated MIC gel was formed in the bottom polymer solution phase and the residual water/IL supernatant was poured off. After vacuum drying the initially hydrated RMIC at 80℃ for more than 24 hours, we obtained the RMIC electrolytes.

Preparation of the Li-loaded MIC: The RMICs were sliced by hand using a scalpel as thin as possible, to obtain a thickness of 250 μm with a standard deviation of 20%. Performance results will improve as we decrease/optimize the thickness of the electrolytes in future investigations. The sliced RMICs were then immersed in the ILEs for > 24 h at room temperature. These operations were completed in an Ar-filled glove box.

^{1}H, ^{19}F and ^{7}Li NMR spectroscopy and pulsed-field-gradient (PFG) NMR diffusometry: A Bruker Avance III widebore 400 MHz (9.4 T) NMR was equipped with a diff60 pulsed-field-gradient diffusion probe having a maximum gradient value of 2000 G/cm (at 33 A) along the Z axis and 5 mm ^{7}Li and 8 mm ^{1}H/^{19}F rf coils. The PGSTE sequence used a π/2 pulse, gradient pulse duration δ of 1 - 2 ms, diffusion times Δ of 10 - 50 ms and the number of scans for each step was adjusted from 16 - 1024 to ensure good signal-to-noise ratio (SNR). 16 gradient steps were applied for each diffusion experiment. All parameters for the NMR diffusometry experiments have been calibrated and optimized as reported earlier.[50] Solid-state NMR analysis was performed for chemical identification of various samples. The LiMIC samples were prepared in glove box and flame sealed without breaking vacuum in a 5 mm NMR tube to a length of 3 cm filling the coil region of the probe completely. Water content of the samples were

examined using ^{1}H NMR to ensure the samples were dry as shown in **Supplementary Fig. 11**. For solid-state NMR, a Bruker Avance III widebore 400 MHz (9.4 T) NMR was equipped with a static High Power HX SSNMR Probe to allow for short high-power excitation pluses to ensure a wide spectral excitation bandwidth. For ^{19}F spectra a single pulse with a 1.1 μs duration at 200 W was used to achieve a tilt angle of 50°. ^{19}F spectra were collected using an acquisition time of 0.0204 s, relaxation delay of 4 *s*, pre-scan delay of 10 μs, and 64 scans. For the ^{7}Li spectra a single pulse with a 2.8 μs duration at 200 W was used to achieve a tilt angle of 90°. ^{7}Li spectra were collected using an acquisition time of 0.0198 *s*, relaxation delay of 10 *s*, pre-scan delay of 10 μs, and 128 scans. All parameters for the solid-state experiments have been calibrated and optimized to ensure integration values of all spectra are precise. All solid-state NMR spectra were conducted at 25 °C.

X-ray diffraction (XRD)*:* XRD experiments were carried out on a Rigaku Oxford Diffraction Xcalibur Nova Single-Crystal Diffractometer equipped with an Onyx CCD detector and a Cu microsource operating at 49.5 kV and 80 mA at room temperature. The RMIC was sliced to a thickness ~ 1 mm and mounted on the edge of a steel pin, such that the gel extended above the steel pin and into the X-ray beam. The sample-to-detector distance was 50 mm, giving data at scattering angle 2θ from 5º to 42º. The sample was rotated 2º along the ϕ direction. For each sample, a total of 6 images each with 30 s exposure time was collected and summed to increase signal-to-noise ratio. The software CrysAlisPro (v1.171.37.35, Rigaku Oxford Diffraction, 2015, Rigaku Corporation, Oxford, UK) was used for data collection and analysis.

Cyclic voltammetry: A stainless steel working electrode and a Li-metal foil counter electrode were employed for cyclic voltammetry. The CV measurements were performed against Li|Li^{+} redox potential.[33] All scans were performed at 25°C with 5 mV s^{-1} scan rate using a Biologic SP-

200 controlled by EC-Lab (ver. 10.40) software.

Symmetric lithium metal coin cells: The coin cells were prepared with CR2032 cases with two 3.2 mm (1/8 inch) diameter lithium electrodes in an Ar-filled glove box. The coin cells were used for impedance spectroscopy and cycling measurements. A VMP3 (BioLogic) system and a Neware system were used for battery testing.

Ionic conductivity: The ionic conductivity was measured via dielectric response over a 1 Hz – 1 MHz frequency range (to emphasize the electrode-electrolyte interfacial resistance) at an amplitude of 20 mV. A temperature scan range 20 °C to 100 °C was selected, and the temperature was controlled by a Eurotherm 2204 temperature controller. Conductivity of the LiMIC was extracted using a value of electrical resistance obtained by fitting the data to an equivalent circuit model using EC-Lab (ver. 10.40) software®. Two heating scans with 10 °C intervals were conducted, and the data shown in this study were extracted from the second heating scan.

Li Transference Number (t_{Li^+}): The transference number was electrochemically determined by direct current (DC) polarization. An AC impedance test was firstly performed over a 0.1 Hz to 1 MHz range to obtain a total resistance R_{cell}. Then the polarization was carried out to obtain a stable current. Cells were polarized at ambient temperature with a constant potential of 10 mV for 2 h.

Dynamic Mechanical Analysis (DMA): The mechanical properties of the composites were investigated at 1Hz frequency using a DMA 8000 (PerkinElmer) from -50 to 200 °C. The sample preparation was finished in a N_2-filled glovebox (H_2O < 100 ppm). The compression mode was used to determine the storage modulus and loss modules of each electrolyte. The test sample was first cooled to −50 °C and then heated to 200 °C at a heating rate of 2 °C/min.

Differential scanning calorimetry (DSC): A Netzsch DSC (214 polyma), calibrated with cyclohexane, was used to investigate the thermal behaviour of the MICs. The heating and cooling rate were 10 °C min^{-1}. Samples were cooled to -100 °C and then three heating scans were followed.

Nanoindentation results were measured at room temperature using a hysitron triboindenter.

Scanning electron microscopy was performed using a JSM IT 300 series microscope and energy dispersive X-ray spectroscopy was measured with an Oxford X-Max 50 mm^2 EDX detector.

References

1 Wang, Y. *et al.* Highly Conductive and Thermally Stable Ion Gels with Tunable Anisotropy and Modulus. *Adv Mater* **28**, 2571-+, doi:10.1002/adma.201505183 (2016).

2 Christie, A. M., Lilley, S. J., Staunton, E., Andreev, Y. G. & Bruce, P. G. Increasing the conductivity of crystalline polymer electrolytes. *Nature* **433**, 50-53, doi:10.1038/nature03186 (2005).

3 Famprikis, T., Canepa, P., Dawson, J. A., Islam, M. S. & Masquelier, C. Fundamentals of inorganic solid-state electrolytes for batteries. *Nature Materials* **18**, 1278-1291, doi:10.1038/s41563-019-0431-3 (2019).

4 Manthiram, A., Yu, X. & Wang, S. Lithium battery chemistries enabled by solid-state electrolytes. *Nature Reviews Materials* **2**, 16103, doi:10.1038/natrevmats.2016.103 (2017).

5 Lu, Y. Y., Tu, Z. Y. & Archer, L. A. Stable lithium electrodeposition in liquid and nanoporous solid electrolytes. *Nature Materials* **13**, 961-969, doi:10.1038/NMAT4041 (2014).

6 Qian, J. F. *et al.* High rate and stable cycling of lithium metal anode. *Nat Commun* **6**, doi:10.1038/Ncomms7362 (2015).

7 Bruce, P. G., Freunberger, S. A., Hardwick, L. J. & Tarascon, J. M. Li-O-2 and Li-S batteries with high energy storage (vol 11, pg 19, 2012). *Nature Materials* **11**, doi:10.1038/NMAT3237 (2012).

8 Krause, A. *et al.* High Area Capacity Lithium-Sulfur Full-cell Battery with Prelitiathed Silicon Nanowire-Carbon Anodes for Long Cycling Stability. *Scientific Reports* **6**, 27982, doi:10.1038/srep27982 (2016).

9 Lu, J. *et al.* A lithium–oxygen battery based on lithium superoxide. *Nature* **529**, 377-382, doi:10.1038/nature16484 (2016).

10 Maier, J. Nanoionics: ion transport and electrochemical storage in confined systems. *Nature Materials* **4**, 805-815, doi:10.1038/nmat1513 (2005).

11 Sakuda, A., Hayashi, A. & Tatsumisago, M. Sulfide Solid Electrolyte with Favorable Mechanical Property for All-Solid-State Lithium Battery. *Scientific Reports* **3**, 2261, doi:10.1038/srep02261 (2013).
12 Elia, G. A. *et al.* An Advanced Lithium–Air Battery Exploiting an Ionic Liquid-Based Electrolyte. *Nano Letters* **14**, 6572-6577, doi:10.1021/nl5031985 (2014).
13 Bostwick, J. E. *et al.* Ion Transport and Mechanical Properties of Non-Crystallizable Molecular Ionic Composite Electrolytes. *Macromolecules* **53**, 1405-1414, doi:10.1021/acs.macromol.9b02125 (2020).
14 Fox, R. J. *et al.* Nanofibrillar Ionic Polymer Composites Enable High-Modulus Ion-Conducting Membranes. *ACS Applied Materials & Interfaces* **11**, 40551-40563, doi:10.1021/acsami.9b10921 (2019).
15 Yu, Z., He, Y. D., Wang, Y., Madsen, L. A. & Qiao, R. Molecular Structure and Dynamics of Ionic Liquids in a Rigid-Rod Polyanion-Based Ion Gel. *Langmuir* **33**, 322-331, doi:10.1021/acs.langmuir.6b03798 (2017).
16 Wang, Y. *et al.* Double helical conformation and extreme rigidity in a rodlike polyelectrolyte. *Nature Communications* **10**, 801, doi:10.1038/s41467-019-08756-3 (2019).
17 Wang, Y., Gao, J., Dingemans, T. J. & Madsen, L. A. Molecular Alignment and Ion Transport in Rigid Rod Polyelectrolyte Solutions. *Macromolecules* **47**, 2984-2992, doi:10.1021/ma500364t (2014).
18 Lodge, T. P. Materials science - A unique platform for materials design. *Science* **321**, 50-51, doi:DOI 10.1126/science.1159652 (2008).
19 Lu, Y. Y., Korf, K., Kambe, Y., Tu, Z. Y. & Archer, L. A. Ionic-Liquid-Nanoparticle Hybrid Electrolytes: Applications in Lithium Metal Batteries. *Angew Chem Int Edit* **53**, 488-492, doi:10.1002/anie.201307137 (2014).
20 Wu, F. *et al.* "Liquid-in-Solid" and "Solid-in-Liquid" Electrolytes with High Rate Capacity and Long Cycling Life for Lithium-Ion Batteries. *Chem Mater* **28**, 848-856, doi:10.1021/acs.chemmater.5b04278 (2016).
21 Armand, M., Endres, F., MacFarlane, D. R., Ohno, H. & Scrosati, B. Ionic-liquid materials for the electrochemical challenges of the future. *Nature Materials* **8**, 621-629, doi:Doi 10.1038/Nmat2448 (2009).
22 Ueki, T. & Watanabe, M. Macromolecules in ionic liquids: Progress, challenges, and opportunities. *Macromolecules* **41**, 3739-3749, doi:Doi 10.1021/Ma800171k (2008).
23 Horowitz, A. I. & Panzer, M. J. High-performance, mechanically compliant silica-based ionogels for electrical energy storage applications. *J Mater Chem* **22**, 16534-16539, doi:10.1039/c2jm33496h (2012).
24 Lodge, T. P. & Ueki, T. Mechanically Tunable, Readily Processable Ion Gels by Self-Assembly of Block Copolymers in Ionic Liquids. *Accounts Chem Res* **49**, 2107-2114, doi:10.1021/acs.accounts.6b00308 (2016).
25 Le Bideau, J., Ducros, J. B., Soudan, P. & Guyomard, D. Solid-State Electrode Materials with Ionic-Liquid Properties for Energy Storage: the Lithium Solid-State Ionic-Liquid Concept. *Adv Funct Mater* **21**, 4073-4078, doi:DOI 10.1002/adfm.201100774 (2011).
26 Bhattacharyya, A. J., Dolle, M. & Maier, J. Improved Li-battery electrolytes by heterogeneous doping of nonaqueous Li-salt solutions. *Electrochem Solid St* **7**, A432-A434, doi:10.1149/1.1808113 (2004).

27 MacFarlane, D. R. & Forsyth, M. Plastic crystal electrolyte materials: New perspectives on solid state ionics. *Adv Mater* **13**, 957-+, doi:Doi 10.1002/1521-4095(200107)13:12/13<957::Aid-Adma957>3.0.Co;2-# (2001).
28 Alarco, P. J., Abu-Lebdeh, Y. & Armand, M. Highly conductive, organic plastic crystals based on pyrazolium imides. *Solid State Ionics* **175**, 717-720, doi:10.1016/j.ssi.2003.10.024 (2004).
29 Matsumoto, H. *et al.* Fast cycling of Li/LiCoO2 cell with low-viscosity ionic liquids based on bis(fluorosulfonyl)imide [FSI](-). *J Power Sources* **160**, 1308-1313, doi:10.1016/j.jpowsour.2006.02.018 (2006).
30 Zaghib, K. *et al.* Safe Li-ion polymer batteries for HEV applications. *J Power Sources* **134**, 124-129, doi:10.1016/j.jpowsour.2004.02.020 (2004).
31 Basile, A., Bhatt, A. I. & O'Mullane, A. P. Stabilizing lithium metal using ionic liquids for long-lived batteries. *Nat Commun* **7**, doi:10.1038/Ncomms11794 (2016).
32 Yoon, H., Howlett, P. C., Best, A. S., Forsyth, M. & MacFarlane, D. R. Fast Charge/Discharge of Li Metal Batteries Using an Ionic Liquid Electrolyte. *J Electrochem Soc* **160**, A1629-A1637, doi:10.1149/2.022310jes (2013).
33 Yoon, H., Best, A. S., Forsyth, M., MacFarlane, D. R. & Howlett, P. C. Physical properties of high Li-ion content N-propyl-N-methylpyrrolidinium bis(fluorosulfonyl)imide based ionic liquid electrolytes. *Phys Chem Chem Phys* **17**, 4656-4663, doi:10.1039/c4cp05333h (2015).
34 Kim, O., Kim, K., Choi, U. H. & Park, M. J. Tuning anhydrous proton conduction in single-ion polymers by crystalline ion channels. *Nat Commun* **9**, 5029, doi:10.1038/s41467-018-07503-4 (2018).
35 Patterson, A. L. The Scherrer Formula for X-Ray Particle Size Determination. *Physical Review* **56**, 978-982, doi:10.1103/PhysRev.56.978 (1939).
36 Levitt, M. H. *Spin Dynamics: Basics of Nuclear Magnetic Resonance*. (Wiley, 2001).
37 Marple, M., Aitken, B., Kim, S. & Sen, S. Fast Li-ion dynamics in stoichiometric Li2S-Ga2Se3-GeSe2 glasses. *Chem Mater* **29**, doi:10.1021/acs.chemmater.7b02858 (2017).
38 Kidd, B. E., Forbey, S. J., Steuber, F. W., Moore, R. B. & Madsen, L. A. Multiscale Lithium and Counterion Transport in an Electrospun Polymer-Gel Electrolyte. *Macromolecules* **48**, 4481-4490, doi:10.1021/acs.macromol.5b00573 (2015).
39 Kidd, B. E., Lingwood, M. D., Lee, M., Gibson, H. W. & Madsen, L. A. Cation and Anion Transport in a Dicationic Imidazolium-Based Plastic Crystal Ion Conductor. *Journal of Physical Chemistry B* **118**, 2176-2185, doi:10.1021/jp4084629 (2014).
40 Lingwood, M. D. *et al.* Unraveling the local energetics of transport in a polymer ion conductor. *Chem Commun* **49**, 4283-4285, doi:10.1039/c2cc37173a (2013).
41 Hou, J. B., Zhang, Z. Y. & Madsen, L. A. Cation/Anion Associations in Ionic Liquids Modulated by Hydration and Ionic Medium. *Journal of Physical Chemistry B* **115**, 4576-4582, doi:10.1021/jp1110899 (2011).
42 Simons, T. J. *et al.* Influence of Zn2+ and Water on the Transport Properties of a Pyrrolidinium Dicyanamide Ionic Liquid. *Journal of Physical Chemistry B* **118**, 4895-4905, doi:10.1021/jp501665g (2014).
43 Jin, L. *et al.* Structure and Transport Properties of a Plastic Crystal Ion Conductor: Diethyl(methyl)(isobutyl)phosphonium Hexafluorophosphate. *Journal of the American Chemical Society* **134**, 9688-9697, doi:10.1021/ja301175v (2012).

44 Zhu, H., MacFarlane, D. R., Pringle, J. M. & Forsyth, M. Organic Ionic Plastic Crystals as Solid-State Electrolytes. *Trends in Chemistry* **1**, 126-140, doi:10.1016/j.trechm.2019.01.002 (2019).
45 MacFarlane, D. R. *et al.* Ionic liquids and their solid-state analogues as materials for energy generation and storage. *Nature Reviews Materials* **1**, 15005, doi:10.1038/natrevmats.2015.5 (2016).
46 Han, X. *et al.* Negating interfacial impedance in garnet-based solid-state Li metal batteries. *Nat Mater* **16**, 572-579, doi:10.1038/nmat4821 (2017).
47 Kerner, M., Plylahan, N., Scheers, J. & Johansson, P. Thermal stability and decomposition of lithium bis(fluorosulfonyl)imide (LiFSI) salts. *RSC Advances* **6**, 23327-23334, doi:10.1039/C5RA25048J (2016).
48 Zhao, Q., Liu, X., Stalin, S., Khan, K. & Archer, L. A. Solid-state polymer electrolytes with in-built fast interfacial transport for secondary lithium batteries. *Nature Energy* **4**, 365-373, doi:10.1038/s41560-019-0349-7 (2019).
49 Gao, J. W. *et al.* Water and sodium transport and liquid crystalline alignment in a sulfonated aramid membrane. *J Membrane Sci* **489**, 194-203, doi:10.1016/j.memsci.2015.03.090 (2015).
50 Li, J., Park, J. K., Moore, R. B. & Madsen, L. A. Linear coupling of alignment with transport in a polymer electrolyte membrane. *Nature Materials* **10**, 507-511, doi:Doi 10.1038/Nmat3048 (2011).

Data availability

All data generated and analyzed in this study are included in this published article and its supplementary information file and are also available from the corresponding author on reasonable request.

Acknowledgements

This work was supported primarily by the US National Science Foundation under awards DMR 1507764 and 1810194 and in part by the US Department of Energy under award EE0008860. We also gratefully thank Prof. Carla Slebodnick at the Virginia Tech Crystallography Lab for assistance with XRD analysis.

Author contributions

YW designed and executed all major experiments and composed and edited article drafts. XW,

RK, LJ, and MF performed and assisted with electrochemistry and impedance experiments and contributed written sections and editing to the article. CJZ performed solid-state NMR experiments and contributed written sections and editing to the article. WHK analyzed the XRD data and contributed written sections to the article. TJD modified and supplied polymer, conceived experiments and contributed written sections and editing to the article. LAM conceived ideas, oversaw experiments, and composed and edited the article.

Solid-state rigid-rod polymer composite electrolytes with nanocrystalline lithium ion pathways

*Ying Wang[1], Curt J. Zanelotti[1], Xiaoen Wang[2], Robert Kerr[2], Liyu Jin[2], Wang Hay Kan[3], Theo J. Dingemans[4], Maria Forsyth[2], and Louis A. Madsen[1]**

1. Department of Chemistry and Macromolecules Innovation Institute
   Virginia Polytechnic Institute and State University
   Blacksburg, Virginia 24061, United States
   E-mail: lmadsen@vt.edu
2. Institute for Frontier Materials and ARC Centre of Excellent for Electromaterials Science
   Deakin University
   Geelong, VIC 3216, Australia
3. China Spallation Neutron Source
   Chinese Academy of Science
   Dongguan, Guangzhou 523803, China
4. Department of Applied Physical Sciences
   University of North Carolina at Chapel Hill
   121 South Road, Chapel Hill, NC27599-3050, United States

Abstract

A critical challenge for next-generation lithium-based batteries lies in development of electrolytes that enable thermal safety along with use of high-energy-density electrodes. We describe molecular ionic composite (MIC) electrolytes based on an aligned liquid crystalline polymer combined with ionic liquids and concentrated Li salt. This high strength (200 MPa) and non-flammable solid electrolyte possesses outstanding Li^+ conductivity (1 $mS \cdot cm^{-1}$ at 25 °C) and electrochemical stability (5.6 V vs $Li|Li^+$) while suppressing dendrite growth and exhibiting low interfacial resistance (32 $\Omega \cdot cm^2$) and overpotentials (≤ 120 mV @ 1 $mA \cdot cm^{-2}$) during Li symmetric cell cycling. A heterogeneous salt doping process modifies a locally ordered polymer-ion assembly to incorporate an inter-grain network filled with defective LiFSI & $LiBF_4$ nanocrystals, strongly enhancing Li^+ conduction. This modular material fabrication platform shows promise for safe and high-energy-density energy storage and conversion applications, incorporating the fast transport of ceramic-like conductors with the superior flexibility of polymer electrolytes.

Solid-state polymer electrolytes (SPEs) have received great attention toward reviving high-energy-density Li-based batteries.[1-4] While Li-ion batteries play an important role in the energy storage landscape due to their relatively high specific energy and power density, they are approaching theoretical limits (≈ 400 $Wh.kg^{-1}$).[5,6] In order to increase capacity of Li-based batteries, researchers have largely focused on new electrode materials. Regarding cathodes, Li-air and Li-sulfur batteries represent leading frontier candidates.[3,7-9] At the anode, Li-metal can replace graphite to increase anode energy density by ~ 10 fold.[5-7] However, electrode advancements require an enabling electrolyte to combat irreversible reactions and dendrite growth during long-term charge/discharge cycling.[7,10] To alleviate these issues, SPEs not only provide mechanical stiffness to block dendrites, but deliver safer (non-flammable) operation compared to liquid electrolytes.[1,10-12] Herein, we describe a solid-state ***molecular ionic composite*** (MIC) electrolyte[1,13-15] based on an extremely rigid double helical sulfonated aromatic polyamide (similar to Kevlar®)[16,17] combined with an ionic liquid (IL) and a Li salt. We can adjust MIC properties widely by changing polymer content, IL type, and metal salt type and loading. Thus, MICs represent a modular material platform with potential to resolve a range of issues in electrolytic materials.

Previous researchers have developed a number of IL-based gel electrolytes (termed "ion gels" or "ionogels") that combine the non-flammability of ILs with a mechanically supporting matrix.[1,18-21] These electrolytes consist of either a polymer matrix embedded with a large volume fraction of IL,[1,22] or an IL inside an inorganic matrix such as SiO_2 and TiO_2.[19,20,23] Potential applications of these gels for high-energy-density Li batteries have been substantially explored.[20,24,25] However, these gels only show practical Li-metal cycling performance when doped with organic electrolytes,[20,25] which improve conductivity but introduce a volatile liquid

that diminishes safety against overheating and fire.[5,6] In this work, we describe solid-state MIC electrolytes that contain no volatile solvents but exhibit high ionic conductivity, beneficial electrode-electrolyte contact and high thermal stability, all while possessing sufficient modulus to serve as the separator in Li-metal batteries. Loading electrolytes with Li salts serves to increase Li-ion conductivity and supply Li^+ for reactions at the electrodes.[2,26-28] Maier et al. have demonstrated that heterogeneous doping and interfacially controlled materials can be used to increase Li^+ conductivity in electrolytes.[10] Christie et al. reported that the presence of the irregularly shaped bis(trifluoromethanesulfonyl)imide ($TFSI^-$) anion disrupts the electrostatic potential around Li^+ thereby enhancing ionic conductivity in a manner analogous to inorganic electrolytes such as $AgBr_{1-x}I_x$.[2] Recently, lithium bis(fluorosulfonyl)imide (LiFSI) has emerged as a promising electrolyte component.[28-30] Furthermore, the FSI^- anion can decompose upon electroreduction to form a stable solid-electrolyte interphase (SEI) that enables reversible cycling with a graphitic anode.[31] In this project, we employ ionic liquid electrolytes (ILEs) containing *N*-propyl-*N*-methylpyrrolidinium (C_3mpyr) FSI mixed with LiFSI (≤ 3.2 mol/kg), which have previously shown Li-metal cycling at high rates.[32,33] By incorporating this ILE into a solid MIC, we demonstrate a highly lithium-dense solid-state electrolyte with potential to suppress Li dendrite growth on Li-metal anodes, enable fast Li^+ transport, and eliminate battery safety concerns.

The Li-loaded MIC (LiMIC) fabrication process requires two steps: (1) Initial polymer-IL network formation, followed by (2) ILE ion exchange to achieve high Li^+ loading. As shown in **Fig. 1a**, we obtain the raw MIC (RMIC), based on an interfacial ion-exchange process between a sulfonated aromatic polyamide, poly-2,2′-disulfonyl-4,4′-benzidine terephthalamide (Li-form PBDT) in H_2O solution and an IL, C_2mimBF_4 (1-ethyl-3-methylimidazolium tetrafluoroborate).[1] PBDT is water-miscible and forms a highly ordered lyotropic nematic liquid crystal (LC) phase at

concentrations > 2 wt%.[16,17] The local parallel packing of charged PBDT rods serves as the assembly template – not only offering mechanical integrity, but also endowing nanoscale structuring in the composite. RMICs are denoted with RMIC-5 and RMIC-15, in which the numbers denote PBDT weight percentage of 5% and 15%. In **Fig. 1b**, we immerse the rigorously dried RMICs in the desired ILE, i.e., C_3mpyrFSI with 50 mol% LiFSI. This serves the dual purposes of lowering the concentration of BF_4^- anions through ion-exchange while also introducing Li^+ ions into the polymer host matrix. By following this two-step fabrication method, we obtain a solid-state MIC electrolyte, denoted LiMIC-5 and LiMIC-15. The key to *Step 1* is that both the IL and LC polyelectrolyte dissolve in the same solvent. *Step 2* allows us to exchange a wide range of IL and Li salt mixtures into the MIC matrix and tailor properties of the product toward Li-metal batteries or other applications. The SEM images of RMICs (**Fig. 1c, d**) show locally aligned PBDT LC grains (μm-scale) interspersed with interconnected grain boundaries with a wide size distribution from nm - μm. This RMIC has mechanical cohesion propagated by a collective "electrostatic network," which effectively arises from templating of the IL through the highly charged and rigid double helical PBDT rods.[13,15] The RMICs are macroscopically isotropic, but display local alignment originating from the rigid PBDT chains, which can be verified using polarized optical microscopy (**Supplementary Fig. 1)**.[1,17]

Fig. 1e-g illustrates the concepts involved in multi-scale organization of the LiMICs. **Fig. 1e** shows the μm-scale structure of this solid electrolyte, incorporating aligned PBDT grains interleaved with a nanocrystalline ionic phase. These nanocrystalline grain boundaries serve as an additional conductive network providing fast Li^+ transport. As shown in **Fig. 1f**, we propose that after ion exchange with ILE, the interconnected boundaries separating the individual PBDT grains allow for higher Li^+ density and faster Li^+ transport as compared to within the grains. **Fig. 1g**

105 further illustrates the morphology and ion distribution in the internally aligned PBDT grains and
106 the nanocrystalline component formed at the grain boundaries. We will illustrate this model in
107 more detail in the following sections based on multi-modal material characterizations.

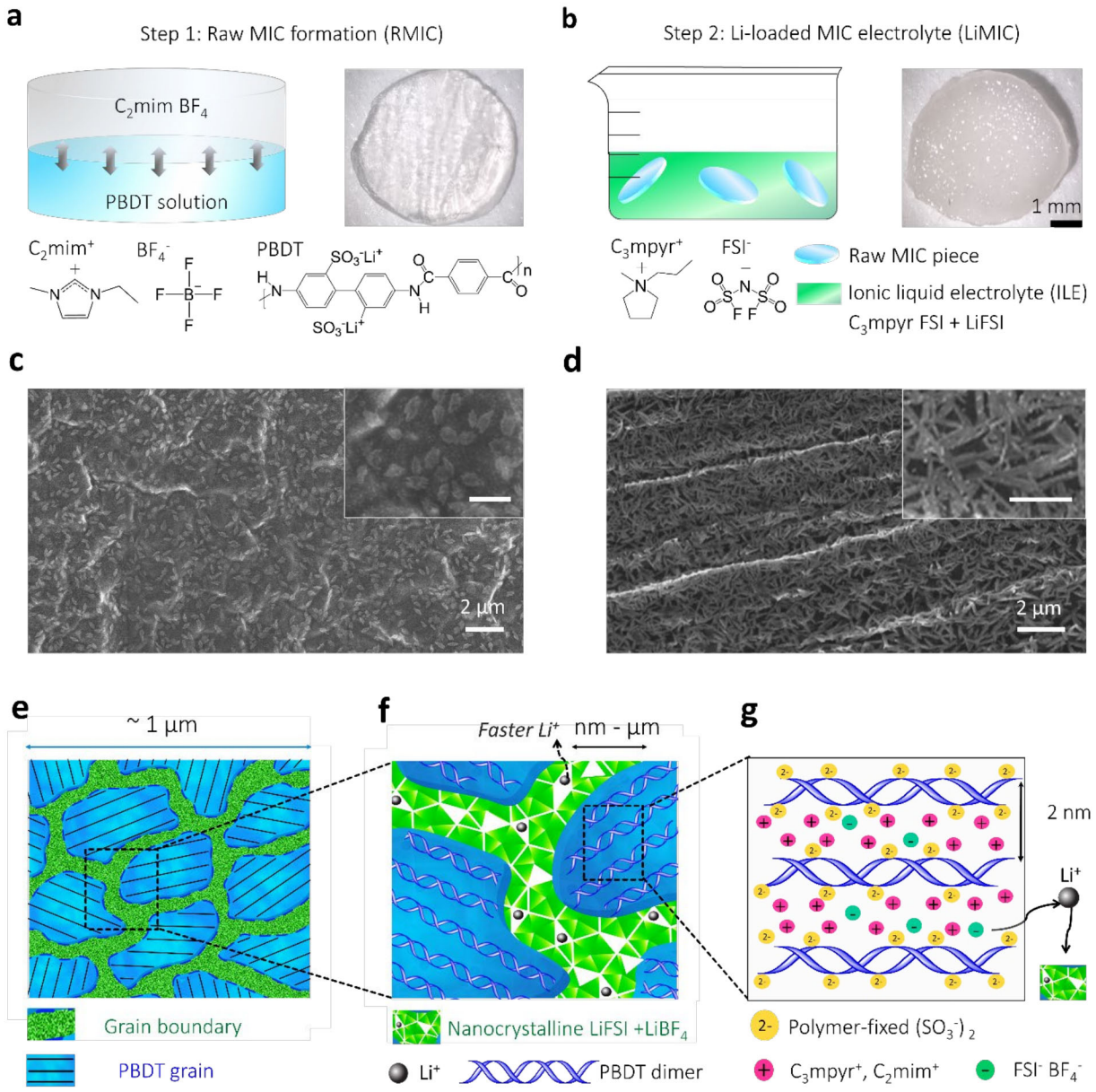

108

109 **Figure 1. Fabrication processes to form Li-loaded MIC electrolytes (LiMICs).** (a) ***Step 1***
110 shows fabrication of the raw MIC (RMIC). Mechanical cohesion in this RMIC arises via
111 electrostatic interactions,[1,13,15] and we obtain this material based on an interfacial ion exchange
112 between a water-soluble IL (e.g., C_2mimBF_4) and an aqueous rigid-rod polyelectrolyte solution

(Li-form PBDT in H_2O). The photograph shows the sliced transparent RMIC sample. (b) ***Step 2*** shows the second ion exchange process wherein we immerse a sliced section of the RMIC into the ILE (C_3mpyrFSI with 50 mol% LiFSI). During the infiltration process, the cation C_3mpyr^+ in the ILE tends to segregate into the PBDT-rich phase,[13,14] as the FSI^- and BF_4^- anions preferentially associate with Li^+ and precipitate out to form a nanoscale heterogeneous structure in the grain boundaries. The photograph shows the sliced iridescent LiMIC sample. (c,d) SEM images for RMIC-5(c) and RMIC-15(d). Higher magnification images are shown in the upper right insets. The scale bar for the insets is 1 μm. The interfaces between individual PBDT grains form the grain boundaries (darker regions). Both the aligned PBDT grains and the grain boundaries contain C_2mimBF_4. (e, f) After ***Step 2***, the grain boundaries become predominantly the condensed salt phase, which consists of nanocrystalline grains that form a conductive network supporting fast Li^+ transport. (g) The morphology of an aligned LC grain contains PBDT double helical rods filled predominantly with mobile IL cations. The distance between PBDT rods is ~ 2 nm.[1,15]

To investigate the nanoscale morphology of these composites, we conducted powder X-ray diffraction (XRD) experiments on the RMIC and LiMIC. As shown in **Fig. 2a**, we observe an amorphous halo with scattering angle 2θ from 12º to 30º for the RMIC, which we assign to the amorphous C_2mimBF_4 in the RMIC. A schematic picture is shown **in Fig. 2b**, where the locally aligned PBDT rods serve as the assembly template for the amorphous IL. The diffraction peaks of the PBDT are overwhelmed by the large volume fraction of IL in the RMIC. By contrast, the XRD of the LiMIC (**Fig. 2c**) shows a heterogeneous structure based on coexistence of the weak amorphous halo and the sharp crystalline reflections. This pattern agrees with the schematic picture shown in **Fig. 2d**, depicting a highly defective nanocrystalline domain formed in-situ between the PBDT grains in the LiMICs. The extracted 1D spectra are shown in **Fig. 2e**. The crystalline peaks (blue line), at first glance, appear to be superimposed diffraction patterns of LiFSI and $LiBF_4$. We also notice that, compared to the amorphous phase, the crystalline phase is the dominant component in the LiMIC, which supports the solid-state NMR (SSNMR) integration results

included in **Supplementary Table 1**, showing that ~ 80% anions (FSI^- and BF_4^-) in LiMIC are localized in the solid crystalline phase. We further use Le Bail refinement to determine the cell parameters for the two potential crystals.[34] **Fig. 2f** shows the fitting results with R-factor for the refinement $R_p = 6.87\%$, which indicates good alignment between the observed diffraction patterns and the simulated phases of LiFSI and $LiBF_4$. The in-situ formed defective crystals of LiFSI and $LiBF_4$ possess preferred orientations, which contribute to the high density of vacancies that promote easier hopping of Li^+ between crystallites. We use the Scherrer equation[35] (**Supplementary Equation 1**) to determine the average crystallite size (19.4 nm) formed in the LiMIC grain boundary regions from the FWHM of the peak at $2\theta = 26.363^\circ$ (012) from the $LiBF_4$ phase. **Table 1** summarizes the Le Bail refinement with cell parameters for the two defective crystals, and both belong to the trigonal crystal structure. These results provide evidence that these nanocrystals are localized in the grain boundaries instead of within PBDT grains, where the distance between PBDT chains is too small to accomodate the nanocrystals.[1,15-17]

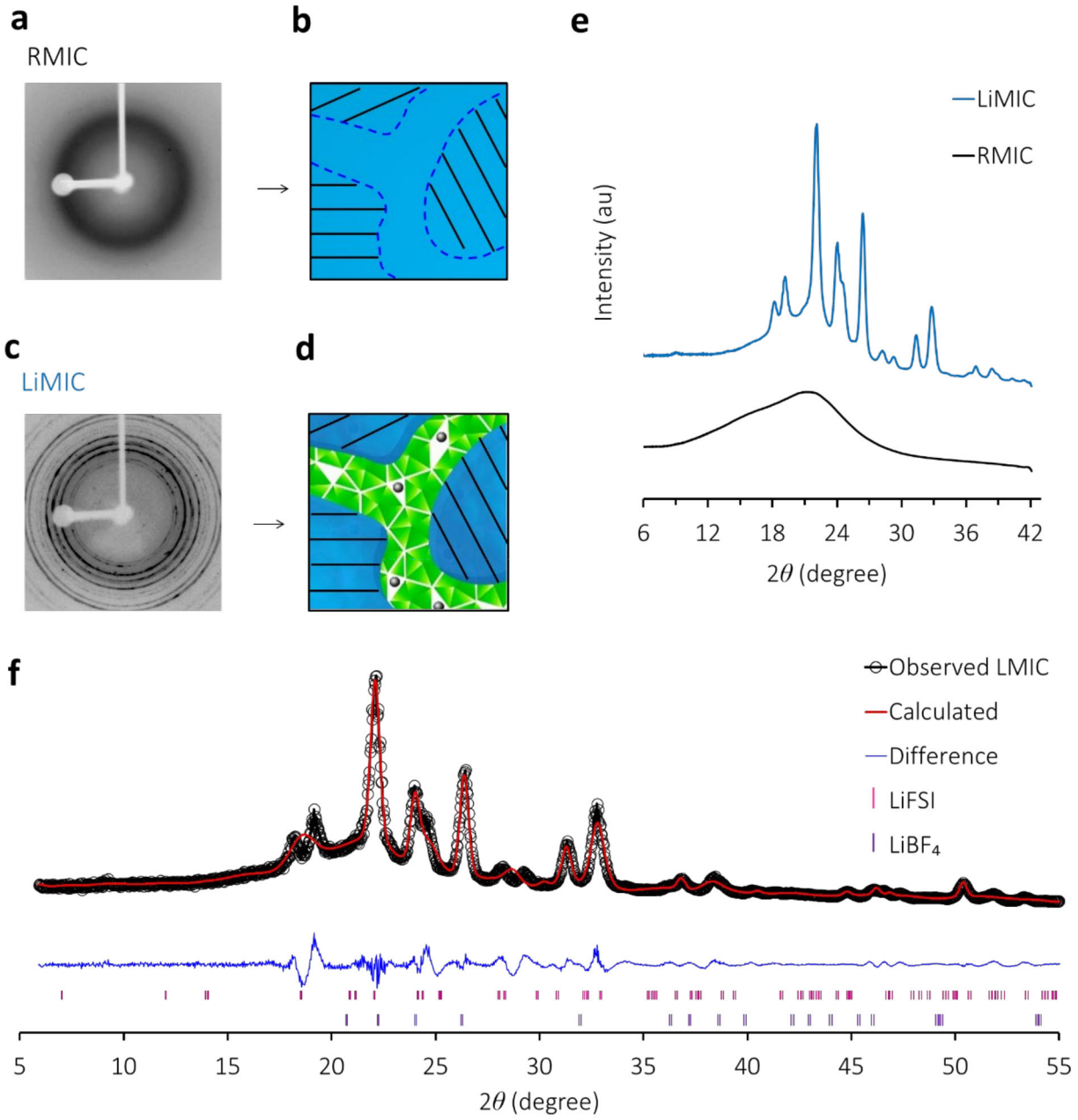

153

154 **Figure 2. X-ray diffraction patterns of RMIC and LiMIC**. (a) Powder XRD pattern for the
155 RMIC. (b) In the RMIC, PBDT LC grains and grain boundaries are filled with amorphous IL as a
156 result of ***Step 1*** of the fabrication process. (c) XRD pattern for the LiMIC. (d) In the LiMIC, there
157 exists an in-situ formed and highly defective nanocrystalline structure between PBDT LC grains.
158 (e) The extracted 1D spectra of the XRD images in (a) and (c). (f) Le Bail refinement results for
159 the LiMIC XRD pattern, which include the observed pattern, the calculated results and the
160 simulation of the in-situ formed nanocrystalline structure of LiFSI and $LiBF_4$.

161

Table 1. Li crystals formed in the LiMIC (R_{wp} = 9.75%, R_p = 6.87%)

LiMIC-15	Phase1 (LiFSI)	Phase2 ($LiBF_4$)
Crystal structure	**Trigonal**	**Trigonal**
Space group	P -3	P 31 2 1
a (Å) (α)	8.513 (90°)	4.9511(90°)
b (Å) (β)	8.513(90°)	4.9511(90°)
c (Å) (γ)	12.610 (120°)	11.112 (120°)
Volume($Å^3$)	779.76	228.02
ICSD	415618	171375

To understand the ion transport and morphology in both RMIC and LiMIC, we first verify the chemical composition of the products, qualitatively and quantitatively, based on ^1H, ^{19}F and ^7Li NMR spectroscopy. **Fig. 3a**, **b**, **c** present key features of these NMR studies. **Fig. 3a** shows ^1H spectra for C_2mim^+ in neat IL and C_3mpyr^+ in ILE (bottom two spectra), and compares ^1H spectra in the RMIC to the LiMIC. The linewidth in the LiMIC (~ 1500 Hz) is much broader compared to the RMIC (~ 100 Hz), which means a factor of ~ 15 faster T_2 spin-spin relaxation, indicating slower motion of IL cations. **Supplementary Fig. 2** shows additional ^1H spectra for RMIC-5 and RMIC-15. SSNMR offers promise for studying the same chemical species in distinct phases, including the grain boundaries and the locally aligned PBDT grains in LiMICs. **Fig. 3b** shows ^{19}F SSNMR spectra for LiMIC (blue line) along with spectra for the reference Li salts (LiFSI and $LiBF_4$). For the LiMIC, we observe a small percentage of mobile BF_4^- with a relatively narrow peak (light blue circle) at -150 ppm. The broad peak underneath (light green semicircle) refers to BF_4^- in the nanocrystalline grain boundaries. Due to its fast internal dynamics, FSI^- appears as only a singlet peak at 60 ppm, which we assign to the superposition of mobile FSI^- in aligned LC grains and solid FSI^- in nanocrystalline grain boundaries. The assignments, assumptions, and quantifications of different ionic species in the LiMICs are summarized in **Supplementary Fig. 3** and **Supplementary Table 1**. **Fig. 3c** compares ^7Li spectra between ILE and LiMIC. The widths and

integration values of the peaks are displayed in **Supplementary Fig. 4**. This single-component 3:4:3 splitting pattern indicates that Li^+ can only exist in either the crystalline grain boundaries or in the PBDT LC grains.[36,37] Based on the XRD, we observe that the Li^+ mainly forms into crystalline phases of LiFSI and $LiBF_4$ in the grain boundaries, thus demonstrating that Li^+ is the dominant cation in the solid nanocrystals, instead of in PBDT LC grains.

Understanding and controlling ion transport, ion associations and Li^+ transport mechanisms in electrolyte materials are critical for development of next-generation battery electrolytes. We can extract the diffusive activation energy (E_a) of the ions present in RMIC and LiMIC electrolytes based on the temperature dependencies of D_{Li^+}, $D_{cations}$ and D_{anions} obtained from NMR diffusometry as shown in **Fig. 3d,e**.[1,38-40] As indicated from the faster T_2 relaxation, we observe that D values for the mobile IL ions in LiMICs are an order of magnitude smaller than those in RMICs, as expected. **Fig. 3f** shows the extracted E_a values for cations and anions in RMICs and LiMICs via the Arrhenius equation. The E_a values for C_2mim^+ and BF_4^- increase with polymer content in the RMICs. This suggests that the density of the PBDT matrix dominates the local energetic barriers that govern ion transport. In addition, compared to the RMICs, the E_a values for cations in the LiMICs almost doubles, whereas E_a for anions show only a slight increment with polymer content. This indicates that the PBDT matrix escalates the local energetic barriers for cation transport in LiMICs, primarily because of stronger associations between the SO_3^- on PBDT chains and C_3mpyr^+. Correspondingly, the schematic picture for the trapped cations within the aligned LC grain is shown in **Fig. 3g.** Conversely, the E_a values for Li^+ in the LiMIC (**Fig. 3h**) decrease with increasing polymer content, indicating smaller local energetic barriers for Li^+ transport compared to the ILE.[13,40] This indicates that a different Li^+ transport mechanism applies for LiMICs. As shown in **Supplementary Table 1**, the concentration of mobile cations (C_2mim^+,

204 C_3mpyr^+) and anions (FSI^-, BF_4^-) in the LiMICs are ~ 6 times lower compared to the RMICs.
205 Meanwhile, LiMICs show an order of magnitude slower diffusion coefficients for the same set of
206 mobile cations and anions. Based on the Nernst–Einstein equation, we suggest that the
207 unexpectedly high conductivity observed in this solid LiMIC electrolyte (see below, Fig. 4a)
208 originates from a fast Li^+ hopping ion transport mechanism in the solid nanocrystalline grain
209 boundaries, as opposed to transport through a liquid-like mobile phase in the PBDT LC
210 grains.[39,41,42] We further determine the Li^+ transference number determined by diffusion ($t_{Li^+\text{-NMR}}$)
211 in LiMICs based on the **Supplementary Equation 2** and include the results in **Supplementary**
212 **Table 1**. **Fig. 3i** depicts the nanocrystalline anions located in the grain boundaries, which we
213 propose give rise to atypically fast Li^+ ion transport.

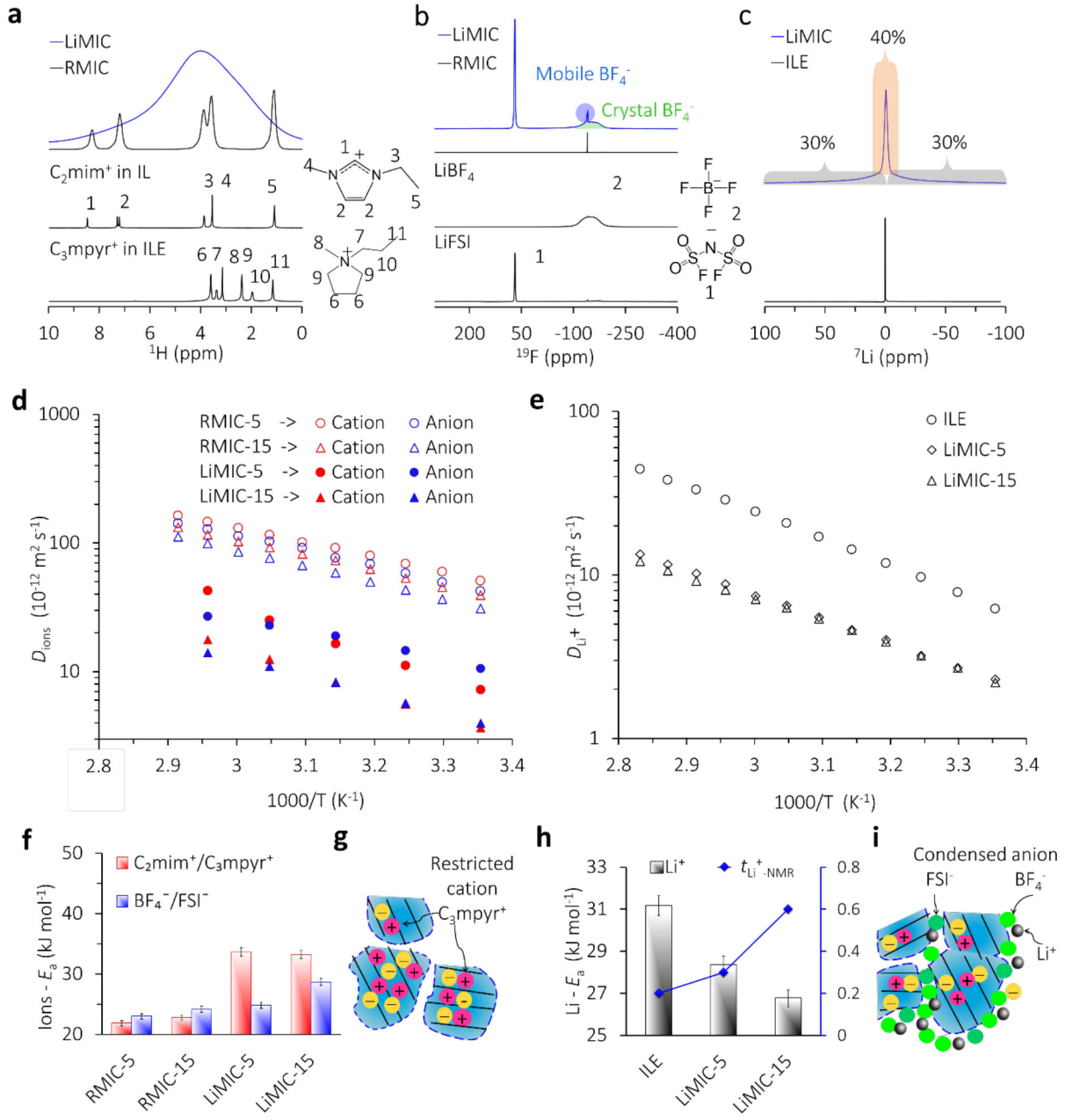

Figure 3. Chemical identification, diffusion coefficients, activation energies and transport mechanism in RMICs and LiMICs. (a) ^{1}H NMR spectra of cations in neat IL (C_2mimBF$_4$), ILE (C_3mpyrFSI with 50 mol% LiFSI), RMIC and LiMIC. The peak in the LiMIC shows overlapping C_3mpyr$^+$ and C_2mim$^+$ signals. (b) ^{19}F NMR spectra of solid LiFSI, solid LiBF$_4$, RMIC and LiMIC. (c) ^{7}Li spectra of liquid ILE and LiMIC. LiMIC shows single anisotropic environment with relative integration values of each broad satellite component being 30% and the narrow central component

being 40% due to the quadrupole splitting of Li. (d) Temperature-dependent $D_{cations}$ and D_{anions} in the RMICs and LiMIC. For LiMICs, $D_{cations}$ represents the average value for C_3mpyr^+ and C_2mim^+. The D_{anions} is the average value for mobile FSI^- and BF_4^-. D_{anions} is the computed weighted average value for the anions based on the mole ratio of mobile FSI^- and BF_4^- as quantified by ^{19}F NMR shown in **Supplementary Fig. 3** and **Supplementary Table 1**. (e) Temperature-dependent D_{Li^+} in ILE and LiMICs. (f) E_a values for cations and anions obtained from Arrhenius fitting of diffusion results. Uncertainties in diffusion are smaller than the marker and uncertainties in E_a are ≈ ±0.5 kJ/mol. (g) Schematic showing C_3mpyr^+ separations into locally aligned LC grains. (h) E_a values for Li^+ obtained from Arrhenius fitting. The blue line compares the measured $t_{Li^+\text{-NMR}}$ in ILE to that in LiMICs. (i) Schematic of the electrolyte structure showing the formation mechanism of nanocrystalline $LiBF_4$ and LiFSI in the grain boundaries.

Building on the RMIC morphology,[1] we propose that the formation mechanism for the heterogeneous structure in LiMICs lies in preferential associations and co-crystallization of specific ions. SO_3^- and C_3mpyr^+ ions should have the weakest associations with other ions due to their size and local charge distributions. Based on XRD and SSNMR results, we expect that FSI^- and BF_4^- have a strong affinity with Li^+ to form a thermodynamically favorable crystalline phase. These nanocrystals (20 nm) form within the grain boundaries when the concentration locally exceeds the saturation point of $LiBF_4$ and LiFSI in the ILE. This leaves the exchanged C_3mpyr^+ and residual C_2mim^+ cations to neutralize predominantly the polymer-fixed SO_3^- anions within the PBDT LC grains. The Li-rich nanocrystalline phase serves as a highly ion-conductive network that can transport Li^+. In these grain boundaries, the space-charge zone and nano-size effects among the polycrystalline $LiBF_4$, LiFSI and aligned crystalline PBDT grains should enhance the vacancy density and conductivity of Li^+, which is consistent with the decreasing E_a of Li^+ obtained from NMR diffusometry. We also note that this nanocrystalline phase likely exhibits features of plastic crystal behavior.[39,43-45] Further investigation of transport mechanisms, grain boundary

heterogeneities, space-charge effects and ion interactions in this heterogeneous structure will provide deeper understanding of these solid electrolytes for future materials design.

Fig. 4a shows ionic conductivities of LiMICs and RMICs as a function of temperature. The exceedingly high σ of LiMIC-5 (2.1 mS·cm^{-1}) and LiMIC-15 (1.5 mS·cm^{-1}) at 25°C surpasses that of state-of-the-art SPEs and even the liquid ILE (0.82 mS·cm^{-1}) we used for ion exchange in *Step 2*.[24,32] In terms of transport energy barriers, LiMICs show higher $E_a(\sigma)$ values compared to RMICs (**Fig. 4b**), which again indicates a distinct transport mechanism in LiMICs. We notice that E_a (Li^+-NMR) in LiMIC is close to the $E_a(\sigma)$ obtained from conductivity. This further indicates that the unexpectedly high conductivity in LiMICs originates from the nanocrystalline conductive network with an ionic alloy ($LiBF_4$ and LiFSI) that forms at the boundaries between individual grains. To supplement this demonstration, we determined the t_{Li^+} based on the steady-state current of the Li symmetric cell assembled with LiMICs as electrolyte and separator in **Fig. 4c**. The corresponding impedance spectra of the cells before polarization are shown in **Supplementary Fig. 5**. The calculation details are included in **Supplementary Table 2** and **Equation S3**. The determined t_{Li^+} in LiMIC-15 (0.60) is much higher compared to the ILE (t_{Li^+} = 0.18).[32] One can then determine the fraction of conductivity due to Li^+ (σ_{Li^+} = 1 mS cm^{-1}) in LiMICs by multiplying the overall conductivity by t_{Li^+}.

We also performed cyclic voltammetry to evaluate the Li plating (negative scan) and stripping (positive scan) behavior in LiMICs. As shown in the 1st cycle in **Fig. 4d**, upon scanning in the positive direction, the electrolyte shows no significant sign of electrochemical decomposition up to 5.6 V vs Li|Li^+. In addition, this electrolyte displays excellent cathodic stability for Li-metal cycling in the following cycles (2nd and 3rd cycles). In **Supplementary Fig. 6**, we observe that the

columbic efficiency of LiMICs increases with cycle number, whereas the ILE shows diminished performance, indicating more effective SEI formation on Li-metal anode when using LiMICs.

Next, we prepared Li|Li symmetric cells and recorded the voltage response for stepped current densities ranging from 0.01 $mA \cdot cm^{-2}$ to 1 $mA \cdot cm^{-2}$. **Fig. 4e** shows the voltage response for LiMIC-15 electrolytes. We observe that LiMIC-15 exhibits stable cycling and can withstand a current density (J) to 1 $mA \cdot cm^{-2}$. This represents state-of-the art performance for SPEs or IL-based electrolyte materials.[5,20] Overpotential is proportional to applied J **(Supplementary Fig. 7),** which follows the Butler-Volmer equation, thus avoiding the possibility of soft shorts.[5,33]

The LMIC electrolyte prepared with the ILE containing the highest concentration of LiFSI (3.2 mol kg^{-1}) shows the most stable cycling performance (**Supplementary Fig. 8** and **Supplementary Table 3**).[32,33] EIS spectra shown in **Fig. 4f** indicate that the SEI resistance increases over the first 40 cycles, then decreases upon further cycling and reduces below that of the initial state at 50 cycles. This is generally associated with an improving SEI layer that forms upon cycling and is commonly observed when cycling Li-metal in this ILE with high salt concentration. Notably, the interfacial resistance for this LiMIC-15 is unusually small, both before (32 $\Omega \cdot cm^{-2}$) and after (17 $\Omega \cdot cm^{-2}$) cycling, compared to other solid-state ion conductors, thereby overcoming the poor electrolyte-electrode contact between Li-metal anode and solid-ion conductor typically observed for, e.g., $Li_{10}GeP_2S_{12}$.[46]

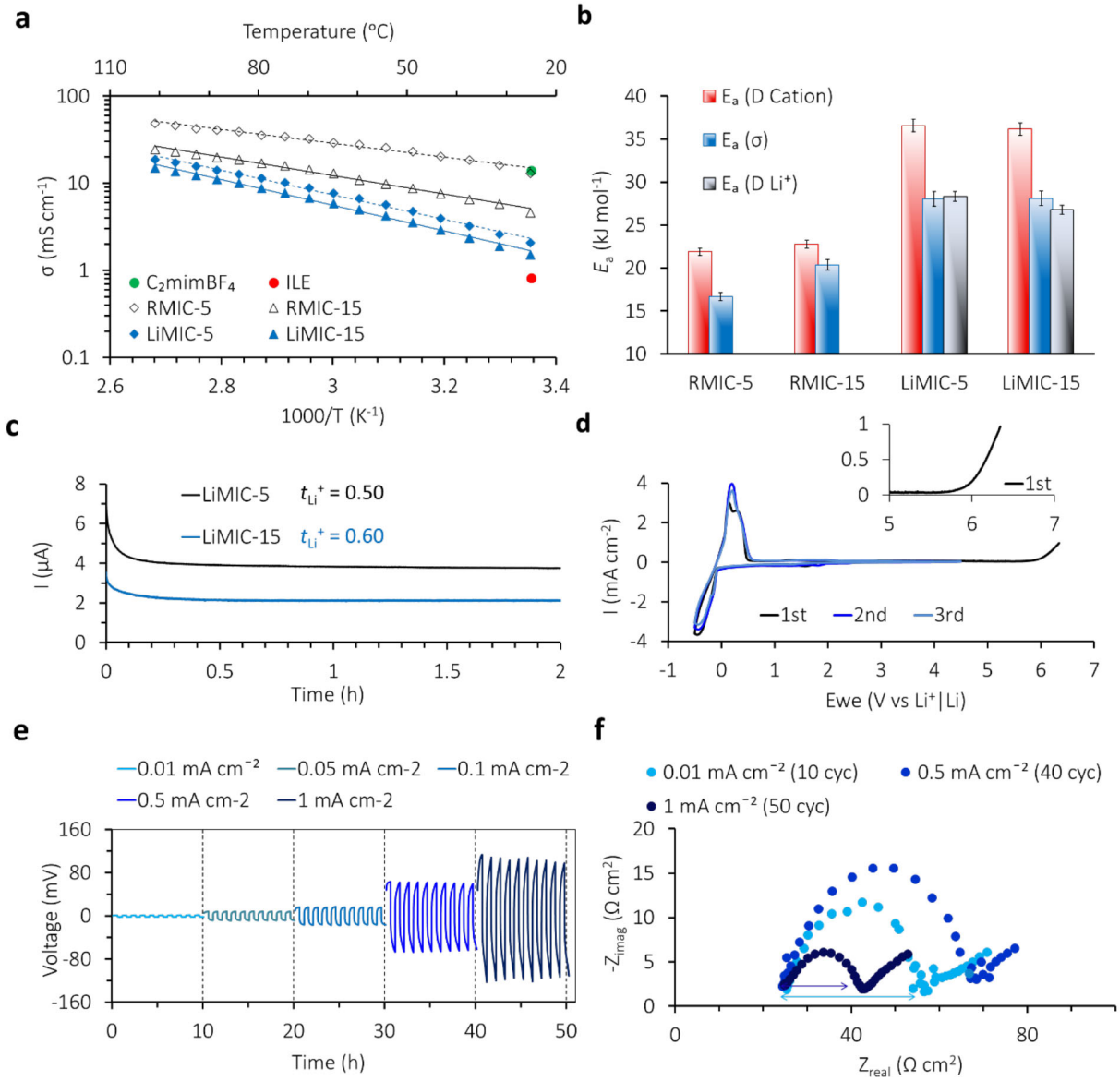

Figure 4. Ionic conductivity, activation energy, Li^+ transference number, electrochemical window, Li symmetric cell cycling performance, and interfacial charge-transfer resistance in MICs. (a) Arrhenius plot used to extract activation energies (E_a) for ionic conductivity within RMICs and LiMICs. The green dot shows the conductivity (σ) of C_2mimBF_4 (25 °C), used for developing RMICs. The ionic conductivity value in ILE is indicated with red dots. (b) Comparison of E_a values obtained from the conductivity results to E_a values of cations and Li^+ based on Arrhenius fitting of NMR diffusometry. (c) Steady-state current in symmetric Li|Li cell using LiMICs under 10 mV polarization. (d) Cyclic voltammetry curves for Li plating and stripping in LiMIC-15 at a sweep rate of 5 mV s^{-1}. Inset plot shows the enlarged view of the 1st cycle in the high voltage range. (e) Cell voltage versus time for a symmetric Li|Li cell using LiMIC-15 at

current densities (J) from 0.01 to 1 mA·cm^{-2} (each cycle lasts 1 h) with changes in J every 10 cycles. (f) Corresponding impedance spectra scanned before variation of J (10 cycles) for the LiMIC-15. The frequency range used is 1Hz – 1MHz.

In addition to the high Li^+ conductivity achieved by LiMICs, we also performed DSC and DMA to better understand their thermal and mechanical stability. As shown in **Fig. 5a**, DSC curves show that C_2mimBF_4 has been mostly exchanged or replaced in LiMICs after *Step 2* of ion exchange. In addition, we observe a glass transition (T_g = -75 °C) for LiFSI, which originates from the LiFSI phase, as reported in this ILE previously.[32,33] The enlarged view on the right displays a broad melting transition (T_m) of LiFSI in LiMICs, consistent with the XRD results showing that there exists a highly defective LiFSI crystalline phase in LiMICs. However, the T_m is not obvious, possibly originating from an endothermic melting process that has been offset by the exothermic degradation of LiFSI, as reported previously.[47] Meanwhile, we employed DMA to investigate the mechanical properties of RMICs and LiMICs between -50°C to 180°C, as shown in **Fig. 5b**. We observe that LiMIC-15 maintains high storage modulus (200 MPa) between -50 to 140 °C, which then drops above 140 °C, near the T_m of LiFSI as well as the degradation temperature for FSI^-.[47] During the heating process, the LiMIC modulus surpasses all previous state-of-the-art SPEs, which usually show poor mechanical strength at temperatures beyond the polymer T_g or T_m.[48] Flammability caused by formation of lithium dendrites represents another key obstacle to safe operation of Li-metal batteries. We included flammability testing results for RMIC in **Supplementary Fig. 9** and observe that RMICs are stable and cannot be ignited under a methane/O_2 flame. Additionally, we carried out nanoindentation experiments to study the microscopic modulus of the MIC materials (**Supplementary Fig. 10**), where we observe a large

distribution of modulus values, reflecting the heterogeneous structure in LiMICs. The median values shown in the boxplots indicate high consistency with macroscopic DMA results.

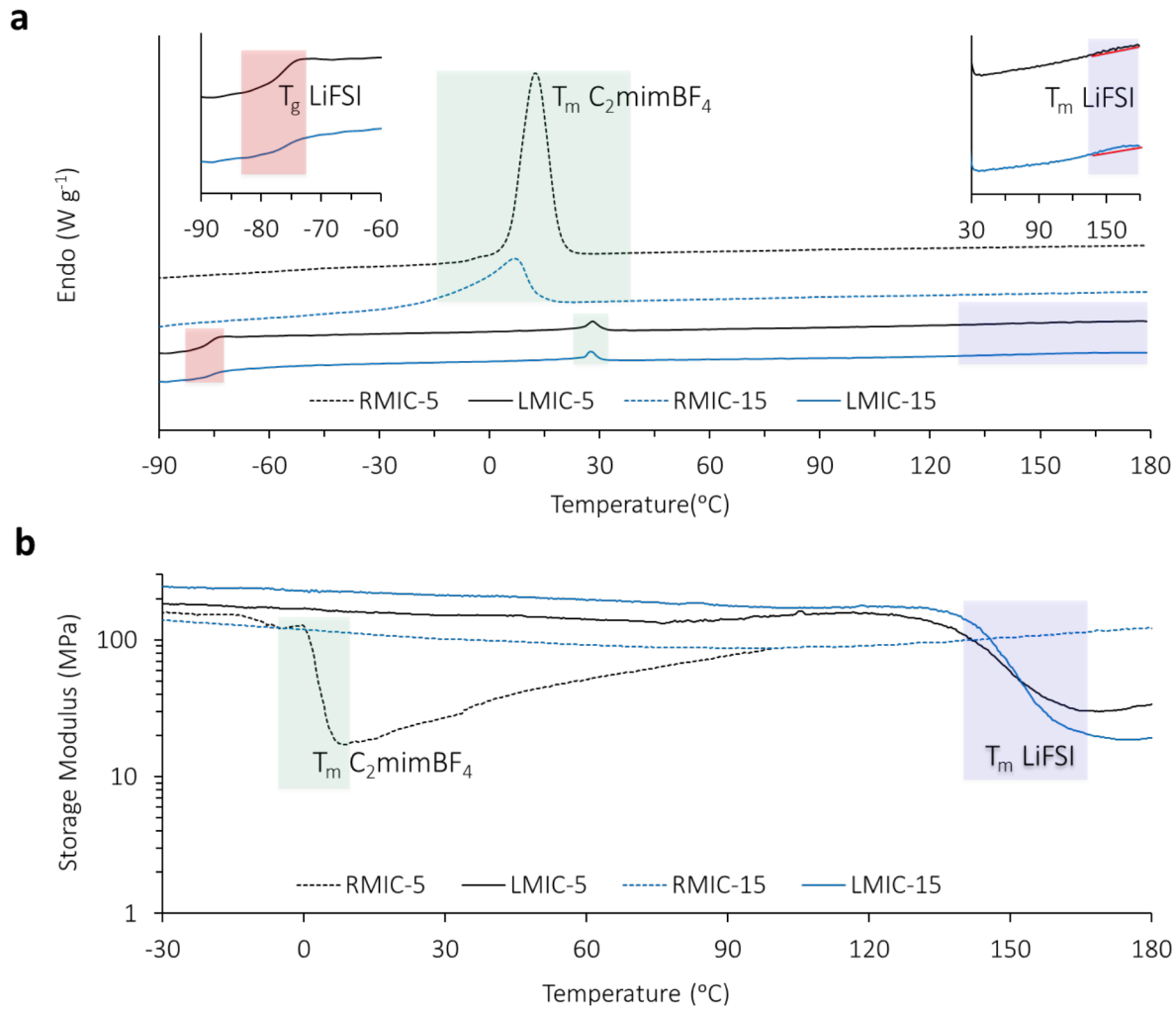

Figure 5. Thermal and mechanical properties of RMICs and LiMICs. (a) DSC shows apparent differences between LiMICs and RMICs. RMICs display the melting (T_m) of IL C_2mimBF_4 at 17 °C, whereas we only see a slight T_m peak for C_2mimBF_4 in LiMICs in agreement with the fact that C_2mimBF_4 has been largely exchanged out. According to peak integration analysis, only < 3% of C_2mimBF_4 remains in the LiMICs. Notably, we do not observe any apparent melting peaks belonging to $C_3mpyrFSI$ or $C_3mpyrBF_4$. The enlarged inset on the left shows the glass transition (T_g) at -75 °C, which originates from the in-situ formed and defective LiFSI phase. The enlarged inset on the right displays the broad melting transition (T_m) of LiFSI in LiMICs. The T_m peak is not obvious, likely because of the opposing thermal transition processes of melting and degradation of LiFSI. (b) DMA shows the mechanical properties of RMICs and LiMICs from -30

°C to 180 °C. RMIC-5 shows a melting drop around the T_m of C_2mimBF_4. LiMICs maintain high modulus (200 MPa) between -50 to 140 °C then start dropping at 140 °C, which is near both the melting and degradation temperatures of LiFSI (140 °C).[47]

In addition to the cycling results in Fig. 4e, **Fig. 6a-b** shows long-term cycling performance of the LiMICs as a function of polymer content and current density (J). Based on comparison between LMIC-5 and LiMIC-15 at increasing J, (0.05, 0.1, 0.2 $mA \cdot cm^{-2}$), we observe that LiMIC-15 (higher polymer content) shows longer cycling stability at all current densities. This suggests that Li dendrite growth is better suppressed by increasing the rigid polymer content. The discussion of short circuit behavior observed for LiMIC-5 is included in Note 10 of supplementary information. **Fig. 6c** demonstrates the cycling stability of LiMIC-15 at $J = 0.2$ $mA \cdot cm^{-2}$. Here, we observe that the cell can cycle without short circuit for > 2000 cycles, which corresponds to 2000 h cycling time and thus removal (and re-plating) of an accumulated total of 1 mm thickness from each Li-metal electrode. Based on the falciform (curved) potential observed in the charging and discharging processes shown in the selected cycles across the long period, we do not observe the unstable voltage profile that typically exists in organic electrolytes at high rates.[32,33] Though overpotential is increasing, we can expect changes to the SEI layer formed on Li-metal during cycling, which is stable enough to suppress Li dendrite growth and prevent short-circuit. Post-cycling SEM of the Li-metal electrode surface (**Fig. 6d, e**) shows a smooth surface devoid of significant dendrites or 'mossy' lithium seen in typical organic electrolyte systems. Peaks from the breakdown products of the FSI^- anion can be seen in the EDX spectra (**Fig. 6f**), which are known to aid in chemically suppressing Li dendrites.[31]

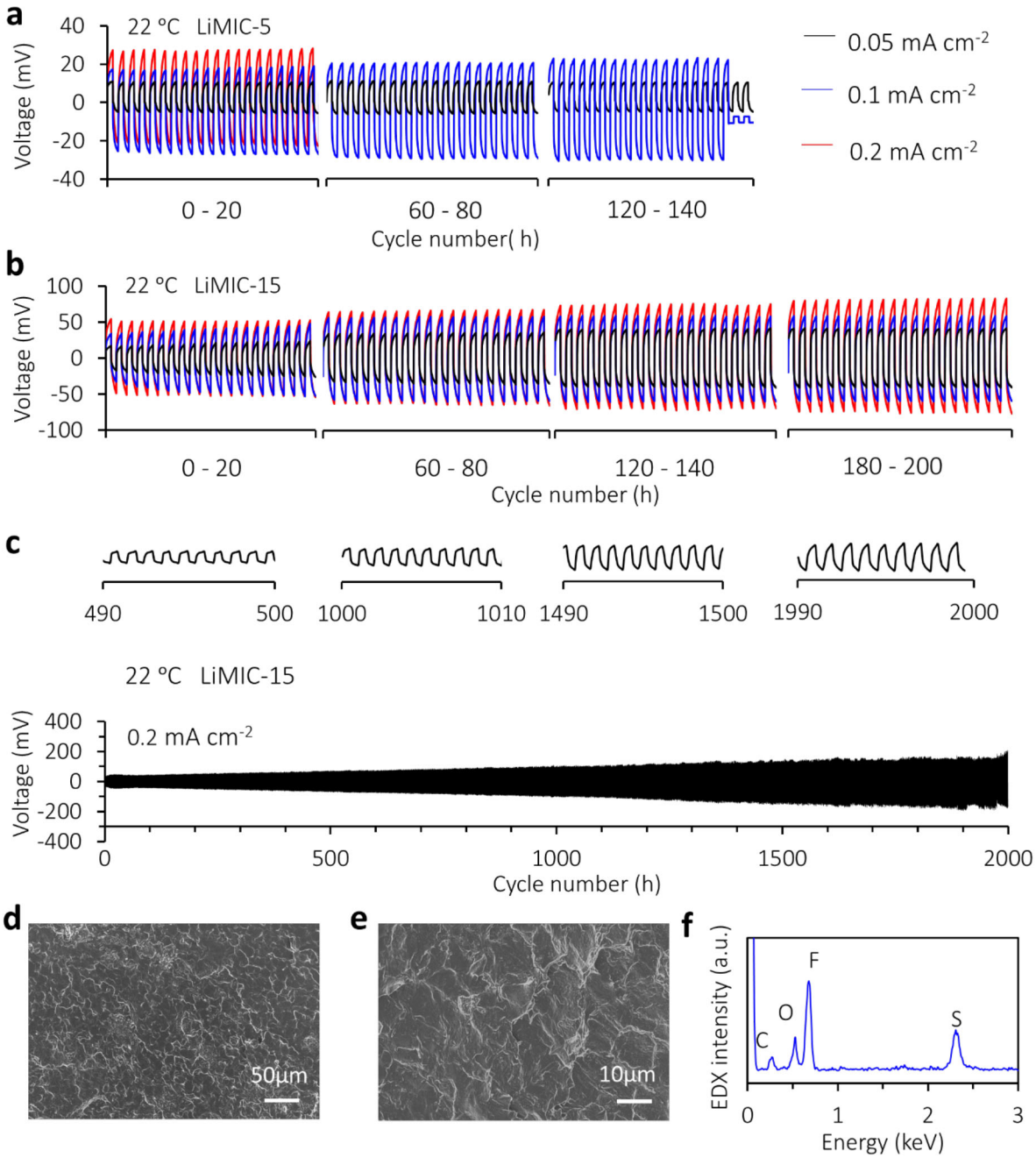

Figure 6. Voltage-time profiles for Li|Li symmetric cells incorporating LiMICs at ambient temperature. 1 cycle = 1 h, or 30 min for each charge and discharge. (a) 0.05 mA·cm^{-2}, 0.1 mA·cm^{-2} , 0.2 mA·cm^{-2} for LiMIC-5, (b) for LiMIC-15. (c) Long-term cycling of LiMIC-15 at current density of 0.2 mA·cm^{-2} with 1 h charge/discharge, insets are profiles for selected cycle numbers in the cycling period. (d, e) SEM images with different magnifications for the disassembled Li-metal electrode after 2000 h long-term cycling in (c) using LiMIC-15 as both electrolyte and separator. (f) EDX spectra of Li-metal surface after long-term cycling.

We have described materials development, mechanisms for ion transport, morphological self-assembly, as well as thermal, mechanical, and electrochemical properties of a new Li-loaded solid-state electrolyte. This inorganic/organic composite material shows immense potential to serve as a next-generation electrolyte for a range of electrochemical devices, suited for frontier battery technologies such as Li-metal, Li-S, or Na-based systems. The fabrication method described enables generation of non-flammable and highly conductive electrolytes with tunable modulus and with selectable metal ion type and varying concentrations. In addition to the initial component IL (C_2mimBF_4) described here, we can also fabricate MICs based on different combinations of ILs and PBDT. **Supplementary Table 4** summarizes the currently accessible MIC fabrication parameter space. Beyond batteries, MICs represent a modular material platform into which we can incorporate a wide range of ionic fluids and salts with an adjustable concentration of the highly charged and rigid double helical PBDT polymer. Such compositional freedom enables the fabrication of MICs with dramatic variations in chemical, mechanical, conductive, electrolytic, and thermal properties to enable applications in the next generation of safe and high-energy-density energy storage devices and beyond.

Methods

Materials: Poly 2,2′-disulfonyl-4,4′-benzidine terephthalamide (PBDT) was synthesized by interfacial condensation polymerization as described previously.[17,49] 1-ethyl-3-methyl imidazolium tetrafluoroborate (C_2mimBF_4, purity > 99%) was purchased from Solvent Innovation GmbH (Cologne, Germany). N-propyl-N-methylpyrrolidinium bis(fluorosulfonyl)imide (C_3mpyrFSI, purity > 99.9%) was purchased from Solvionic. Lithium bis(fluorosulfonyl)imide (LiFSI, purity >99.5%) was sourced from Suzhou Fluolyte Co., Ltd., China. Lithium metal was sourced from China Energy Lithium Co. Ltd. (purity > 99.9%). IL electrolytes (ILEs) in this paper

were prepared by adding the prescribed amount of LiFSI to C_3mpyrFSI IL at room temperature in an Ar-filled glove box (< 0 ppm O_2 and < 10 ppm H_2O).

Preparation of the RMIC: C_2mimBF_4 with the same volume as the (Li-counterion) PBDT seed aqueous solution was slowly pipetted on top of each solution. After 24 hours ion exchange, the hydrated MIC gel was formed in the bottom polymer solution phase and the residual water/IL supernatant was poured off. After vacuum drying the initially hydrated RMIC at 80℃ for more than 24 hours, we obtained the RMIC electrolytes.

Preparation of the Li-loaded MIC: The RMICs were sliced by hand using a scalpel as thin as possible, to obtain a thickness of 250 μm with a standard deviation of 20%. Performance results will improve as we decrease/optimize the thickness of the electrolytes in future investigations. The sliced RMICs were then immersed in the ILEs for > 24 h at room temperature. These operations were completed in an Ar-filled glove box.

^1H, ^{19}F and ^7Li NMR spectroscopy and pulsed-field-gradient (PFG) NMR diffusometry: A Bruker Avance III widebore 400 MHz (9.4 T) NMR was equipped with a diff60 pulsed-field-gradient diffusion probe having a maximum gradient value of 2000 G/cm (at 33 A) along the Z axis and 5 mm ^{7}Li and 8 mm ^{1}H/^{19}F rf coils. The PGSTE sequence used a $\pi/2$ pulse, gradient pulse duration δ of 1 - 2 ms, diffusion times Δ of 10 - 50 ms and the number of scans for each step was adjusted from 16 - 1024 to ensure good signal-to-noise ratio (SNR). 16 gradient steps were applied for each diffusion experiment. All parameters for the NMR diffusometry experiments have been calibrated and optimized as reported earlier.[50] Solid-state NMR analysis was performed for chemical identification of various samples. The LiMIC samples were prepared in glove box and flame sealed without breaking vacuum in a 5 mm NMR tube to a length of 3 cm filling the coil region of the probe completely. Water content of the samples were examined using ^{1}H NMR to

ensure the samples were dry as shown in **Supplementary Fig. 11**. For solid-state NMR, a Bruker Avance III widebore 400 MHz (9.4 T) NMR was equipped with a static High Power HX SSNMR Probe to allow for short high-power excitation pluses to ensure a wide spectral excitation bandwidth. For ^{19}F spectra a single pulse with a 1.1 μs duration at 200 W was used to achieve a tilt angle of 50°. ^{19}F spectra were collected using an acquisition time of 0.0204 s, relaxation delay of 4 *s*, pre-scan delay of 10 μs, and 64 scans. For the ^{7}Li spectra a single pulse with a 2.8 μs duration at 200 W was used to achieve a tilt angle of 90°. ^{7}Li spectra were collected using an acquisition time of 0.0198 *s*, relaxation delay of 10 *s*, pre-scan delay of 10 μs, and 128 scans. All parameters for the solid-state experiments have been calibrated and optimized to ensure integration values of all spectra are precise. All solid-state NMR spectra were conducted at 25 °C.

X-ray diffraction (XRD)*:* XRD experiments were carried out on a Rigaku Oxford Diffraction Xcalibur Nova Single-Crystal Diffractometer equipped with an Onyx CCD detector and a Cu microsource operating at 49.5 kV and 80 mA at room temperature. The RMIC was sliced to a thickness ~ 1 mm and mounted on the edge of a steel pin, such that the gel extended above the steel pin and into the X-ray beam. The sample-to-detector distance was 50 mm, giving data at scattering angle 2θ from 5º to 42º. The sample was rotated 2º along the ϕ direction. For each sample, a total of 6 images each with 30 s exposure time was collected and summed to increase signal-to-noise ratio. The software CrysAlisPro (v1.171.37.35, Rigaku Oxford Diffraction, 2015, Rigaku Corporation, Oxford, UK) was used for data collection and analysis.

Cyclic voltammetry: A stainless steel working electrode and a Li-metal foil counter electrode were employed for cyclic voltammetry. The CV measurements were performed against $Li|Li^{+}$ redox potential.[33] All scans were performed at 25°C with 5 mV s^{-1} scan rate using a Biologic SP-200 controlled by EC-Lab (ver. 10.40) software.

Symmetric lithium metal coin cells: The coin cells were prepared with CR2032 cases with two 3.2 mm (1/8 inch) diameter lithium electrodes in an Ar-filled glove box. The coin cells were used for impedance spectroscopy and cycling measurements. A VMP3 (BioLogic) system and a Neware system were used for battery testing.

Ionic conductivity: The ionic conductivity was measured via dielectric response over a 1 Hz – 1 MHz frequency range (to emphasize the electrode-electrolyte interfacial resistance) at an amplitude of 20 mV. A temperature scan range 20 °C to 100 °C was selected, and the temperature was controlled by a Eurotherm 2204 temperature controller. Conductivity of the LiMIC was extracted using a value of electrical resistance obtained by fitting the data to an equivalent circuit model using EC-Lab (ver. 10.40) software®. Two heating scans with 10 °C intervals were conducted, and the data shown in this study were extracted from the second heating scan.

Li Transference Number (t_{Li^+}): The transference number was electrochemically determined by direct current (DC) polarization. An AC impedance test was firstly performed over a 0.1 Hz to 1 MHz range to obtain a total resistance R_{cell}. Then the polarization was carried out to obtain a stable current. Cells were polarized at ambient temperature with a constant potential of 10 mV for 2 h.

Dynamic Mechanical Analysis (DMA): The mechanical properties of the composites were investigated at 1Hz frequency using a DMA 8000 (PerkinElmer) from -50 to 200 °C. The sample preparation was finished in a N_2-filled glovebox (H_2O < 100 ppm). The compression mode was used to determine the storage modulus and loss modules of each electrolyte. The test sample was first cooled to −50 °C and then heated to 200 °C at a heating rate of 2 °C/min.

Differential scanning calorimetry (DSC): A Netzsch DSC (214 polyma), calibrated with cyclohexane, was used to investigate the thermal behaviour of the MICs. The heating and cooling rate were 10 °C min^{-1}. Samples were cooled to -100 °C and then three heating scans were followed.

Nanoindentation results were measured at room temperature using a hysitron triboindenter.

Scanning electron microscopy was performed using a JSM IT 300 series microscope and energy dispersive X-ray spectroscopy was measured with an Oxford X-Max 50 mm^2 EDX detector.

References

1 Wang, Y. *et al.* Highly Conductive and Thermally Stable Ion Gels with Tunable Anisotropy and Modulus. *Adv Mater* **28**, 2571-+, doi:10.1002/adma.201505183 (2016).

2 Christie, A. M., Lilley, S. J., Staunton, E., Andreev, Y. G. & Bruce, P. G. Increasing the conductivity of crystalline polymer electrolytes. *Nature* **433**, 50-53, doi:10.1038/nature03186 (2005).

3 Famprikis, T., Canepa, P., Dawson, J. A., Islam, M. S. & Masquelier, C. Fundamentals of inorganic solid-state electrolytes for batteries. *Nature Materials* **18**, 1278-1291, doi:10.1038/s41563-019-0431-3 (2019).

4 Manthiram, A., Yu, X. & Wang, S. Lithium battery chemistries enabled by solid-state electrolytes. *Nature Reviews Materials* **2**, 16103, doi:10.1038/natrevmats.2016.103 (2017).

5 Lu, Y. Y., Tu, Z. Y. & Archer, L. A. Stable lithium electrodeposition in liquid and nanoporous solid electrolytes. *Nature Materials* **13**, 961-969, doi:10.1038/NMAT4041 (2014).

6 Qian, J. F. *et al.* High rate and stable cycling of lithium metal anode. *Nat Commun* **6**, doi:10.1038/Ncomms7362 (2015).

7 Bruce, P. G., Freunberger, S. A., Hardwick, L. J. & Tarascon, J. M. Li-O-2 and Li-S batteries with high energy storage (vol 11, pg 19, 2012). *Nature Materials* **11**, doi:10.1038/NMAT3237 (2012).

8 Krause, A. *et al.* High Area Capacity Lithium-Sulfur Full-cell Battery with Prelitiathed Silicon Nanowire-Carbon Anodes for Long Cycling Stability. *Scientific Reports* **6**, 27982, doi:10.1038/srep27982 (2016).

9 Lu, J. *et al.* A lithium–oxygen battery based on lithium superoxide. *Nature* **529**, 377-382, doi:10.1038/nature16484 (2016).

10 Maier, J. Nanoionics: ion transport and electrochemical storage in confined systems. *Nature Materials* **4**, 805-815, doi:10.1038/nmat1513 (2005).

11 Sakuda, A., Hayashi, A. & Tatsumisago, M. Sulfide Solid Electrolyte with Favorable Mechanical Property for All-Solid-State Lithium Battery. *Scientific Reports* **3**, 2261, doi:10.1038/srep02261 (2013).

12 Elia, G. A. *et al.* An Advanced Lithium–Air Battery Exploiting an Ionic Liquid-Based Electrolyte. *Nano Letters* **14**, 6572-6577, doi:10.1021/nl5031985 (2014).

13 Bostwick, J. E. *et al.* Ion Transport and Mechanical Properties of Non-Crystallizable Molecular Ionic Composite Electrolytes. *Macromolecules* **53**, 1405-1414, doi:10.1021/acs.macromol.9b02125 (2020).

14 Fox, R. J. *et al.* Nanofibrillar Ionic Polymer Composites Enable High-Modulus Ion-Conducting Membranes. *ACS Applied Materials & Interfaces* **11**, 40551-40563, doi:10.1021/acsami.9b10921 (2019).

15 Yu, Z., He, Y. D., Wang, Y., Madsen, L. A. & Qiao, R. Molecular Structure and Dynamics of Ionic Liquids in a Rigid-Rod Polyanion-Based Ion Gel. *Langmuir* **33**, 322-331, doi:10.1021/acs.langmuir.6b03798 (2017).
16 Wang, Y. *et al.* Double helical conformation and extreme rigidity in a rodlike polyelectrolyte. *Nature Communications* **10**, 801, doi:10.1038/s41467-019-08756-3 (2019).
17 Wang, Y., Gao, J., Dingemans, T. J. & Madsen, L. A. Molecular Alignment and Ion Transport in Rigid Rod Polyelectrolyte Solutions. *Macromolecules* **47**, 2984-2992, doi:10.1021/ma500364t (2014).
18 Lodge, T. P. Materials science - A unique platform for materials design. *Science* **321**, 50-51, doi:DOI 10.1126/science.1159652 (2008).
19 Lu, Y. Y., Korf, K., Kambe, Y., Tu, Z. Y. & Archer, L. A. Ionic-Liquid-Nanoparticle Hybrid Electrolytes: Applications in Lithium Metal Batteries. *Angew Chem Int Edit* **53**, 488-492, doi:10.1002/anie.201307137 (2014).
20 Wu, F. *et al.* "Liquid-in-Solid" and "Solid-in-Liquid" Electrolytes with High Rate Capacity and Long Cycling Life for Lithium-Ion Batteries. *Chem Mater* **28**, 848-856, doi:10.1021/acs.chemmater.5b04278 (2016).
21 Armand, M., Endres, F., MacFarlane, D. R., Ohno, H. & Scrosati, B. Ionic-liquid materials for the electrochemical challenges of the future. *Nature Materials* **8**, 621-629, doi:Doi 10.1038/Nmat2448 (2009).
22 Ueki, T. & Watanabe, M. Macromolecules in ionic liquids: Progress, challenges, and opportunities. *Macromolecules* **41**, 3739-3749, doi:Doi 10.1021/Ma800171k (2008).
23 Horowitz, A. I. & Panzer, M. J. High-performance, mechanically compliant silica-based ionogels for electrical energy storage applications. *J Mater Chem* **22**, 16534-16539, doi:10.1039/c2jm33496h (2012).
24 Lodge, T. P. & Ueki, T. Mechanically Tunable, Readily Processable Ion Gels by Self-Assembly of Block Copolymers in Ionic Liquids. *Accounts Chem Res* **49**, 2107-2114, doi:10.1021/acs.accounts.6b00308 (2016).
25 Le Bideau, J., Ducros, J. B., Soudan, P. & Guyomard, D. Solid-State Electrode Materials with Ionic-Liquid Properties for Energy Storage: the Lithium Solid-State Ionic-Liquid Concept. *Adv Funct Mater* **21**, 4073-4078, doi:DOI 10.1002/adfm.201100774 (2011).
26 Bhattacharyya, A. J., Dolle, M. & Maier, J. Improved Li-battery electrolytes by heterogeneous doping of nonaqueous Li-salt solutions. *Electrochem Solid St* **7**, A432-A434, doi:10.1149/1.1808113 (2004).
27 MacFarlane, D. R. & Forsyth, M. Plastic crystal electrolyte materials: New perspectives on solid state ionics. *Adv Mater* **13**, 957-+, doi:Doi 10.1002/1521-4095(200107)13:12/13<957::Aid-Adma957>3.0.Co;2-# (2001).
28 Alarco, P. J., Abu-Lebdeh, Y. & Armand, M. Highly conductive, organic plastic crystals based on pyrazolium imides. *Solid State Ionics* **175**, 717-720, doi:10.1016/j.ssi.2003.10.024 (2004).
29 Matsumoto, H. *et al.* Fast cycling of Li/LiCoO2 cell with low-viscosity ionic liquids based on bis(fluorosulfonyl)imide [FSI](-). *J Power Sources* **160**, 1308-1313, doi:10.1016/j.jpowsour.2006.02.018 (2006).
30 Zaghib, K. *et al.* Safe Li-ion polymer batteries for HEV applications. *J Power Sources* **134**, 124-129, doi:10.1016/j.jpowsour.2004.02.020 (2004).

31 Basile, A., Bhatt, A. I. & O'Mullane, A. P. Stabilizing lithium metal using ionic liquids for long-lived batteries. *Nat Commun* **7**, doi:10.1038/Ncomms11794 (2016).

32 Yoon, H., Howlett, P. C., Best, A. S., Forsyth, M. & MacFarlane, D. R. Fast Charge/Discharge of Li Metal Batteries Using an Ionic Liquid Electrolyte. *J Electrochem Soc* **160**, A1629-A1637, doi:10.1149/2.022310jes (2013).

33 Yoon, H., Best, A. S., Forsyth, M., MacFarlane, D. R. & Howlett, P. C. Physical properties of high Li-ion content N-propyl-N-methylpyrrolidinium bis(fluorosulfonyl)imide based ionic liquid electrolytes. *Phys Chem Chem Phys* **17**, 4656-4663, doi:10.1039/c4cp05333h (2015).

34 Kim, O., Kim, K., Choi, U. H. & Park, M. J. Tuning anhydrous proton conduction in single-ion polymers by crystalline ion channels. *Nat Commun* **9**, 5029, doi:10.1038/s41467-018-07503-4 (2018).

35 Patterson, A. L. The Scherrer Formula for X-Ray Particle Size Determination. *Physical Review* **56**, 978-982, doi:10.1103/PhysRev.56.978 (1939).

36 Levitt, M. H. *Spin Dynamics: Basics of Nuclear Magnetic Resonance*. (Wiley, 2001).

37 Marple, M., Aitken, B., Kim, S. & Sen, S. Fast Li-ion dynamics in stoichiometric Li2S-Ga2Se3-GeSe2 glasses. *Chem Mater* **29**, doi:10.1021/acs.chemmater.7b02858 (2017).

38 Kidd, B. E., Forbey, S. J., Steuber, F. W., Moore, R. B. & Madsen, L. A. Multiscale Lithium and Counterion Transport in an Electrospun Polymer-Gel Electrolyte. *Macromolecules* **48**, 4481-4490, doi:10.1021/acs.macromol.5b00573 (2015).

39 Kidd, B. E., Lingwood, M. D., Lee, M., Gibson, H. W. & Madsen, L. A. Cation and Anion Transport in a Dicationic Imidazolium-Based Plastic Crystal Ion Conductor. *Journal of Physical Chemistry B* **118**, 2176-2185, doi:10.1021/jp4084629 (2014).

40 Lingwood, M. D. *et al.* Unraveling the local energetics of transport in a polymer ion conductor. *Chem Commun* **49**, 4283-4285, doi:10.1039/c2cc37173a (2013).

41 Hou, J. B., Zhang, Z. Y. & Madsen, L. A. Cation/Anion Associations in Ionic Liquids Modulated by Hydration and Ionic Medium. *Journal of Physical Chemistry B* **115**, 4576-4582, doi:10.1021/jp1110899 (2011).

42 Simons, T. J. *et al.* Influence of Zn2+ and Water on the Transport Properties of a Pyrrolidinium Dicyanamide Ionic Liquid. *Journal of Physical Chemistry B* **118**, 4895-4905, doi:10.1021/jp501665g (2014).

43 Jin, L. *et al.* Structure and Transport Properties of a Plastic Crystal Ion Conductor: Diethyl(methyl)(isobutyl)phosphonium Hexafluorophosphate. *Journal of the American Chemical Society* **134**, 9688-9697, doi:10.1021/ja301175v (2012).

44 Zhu, H., MacFarlane, D. R., Pringle, J. M. & Forsyth, M. Organic Ionic Plastic Crystals as Solid-State Electrolytes. *Trends in Chemistry* **1**, 126-140, doi:10.1016/j.trechm.2019.01.002 (2019).

45 MacFarlane, D. R. *et al.* Ionic liquids and their solid-state analogues as materials for energy generation and storage. *Nature Reviews Materials* **1**, 15005, doi:10.1038/natrevmats.2015.5 (2016).

46 Han, X. *et al.* Negating interfacial impedance in garnet-based solid-state Li metal batteries. *Nat Mater* **16**, 572-579, doi:10.1038/nmat4821 (2017).

47 Kerner, M., Plylahan, N., Scheers, J. & Johansson, P. Thermal stability and decomposition of lithium bis(fluorosulfonyl)imide (LiFSI) salts. *RSC Advances* **6**, 23327-23334, doi:10.1039/C5RA25048J (2016).

48 Zhao, Q., Liu, X., Stalin, S., Khan, K. & Archer, L. A. Solid-state polymer electrolytes with in-built fast interfacial transport for secondary lithium batteries. *Nature Energy* **4**, 365-373, doi:10.1038/s41560-019-0349-7 (2019).
49 Gao, J. W. *et al.* Water and sodium transport and liquid crystalline alignment in a sulfonated aramid membrane. *J Membrane Sci* **489**, 194-203, doi:10.1016/j.memsci.2015.03.090 (2015).
50 Li, J., Park, J. K., Moore, R. B. & Madsen, L. A. Linear coupling of alignment with transport in a polymer electrolyte membrane. *Nature Materials* **10**, 507-511, doi:Doi 10.1038/Nmat3048 (2011).

Data availability

All data generated and analyzed in this study are included in this published article and its supplementary information file and are also available from the corresponding author on reasonable request.

Acknowledgements

This work was supported primarily by the US National Science Foundation under awards DMR 1507764 and 1810194 and in part by the US Department of Energy under award EE0008860. We also gratefully thank Prof. Carla Slebodnick at the Virginia Tech Crystallography Lab for assistance with XRD analysis.

Author contributions

YW designed and executed all major experiments and composed and edited article drafts. XW, RK, LJ, and MF performed and assisted with electrochemistry and impedance experiments and contributed written sections and editing to the article. CJZ performed solid-state NMR experiments and contributed written sections and editing to the article. WHK analyzed the XRD data and contributed written sections to the article. TJD modified and supplied polymer, conceived experiments and contributed written sections and editing to the article. LAM conceived ideas, oversaw experiments, and composed and edited the article.